Yeast cells reveal the misfolding and the cellular mislocalisation of the human BRCA1 protein

Pierre Thouvenot, Lou Fourrière, Elodie Dardillac, Barbara Ben Yamin, Aurianne Lescure, Vincent Lejour, Xavier Heiligenstein, Jean-Baptiste Boulé, Maryse Romao, Graça Raposo-Benedetti, et al.

Yeast cells reveal the misfolding and the cellular mislocalisation of the human BRCA1 protein

Pierre Thouvenot,[1,2] Lou Fourrière,[1,2] Elodie Dardillac,[3] Barbara Ben Yamin,[1,2] Aurianne Lescure,[1,2] Vincent Lejour,[1,2] Xavier Heiligenstein,[2,4] Jean-Baptiste Boulé,[1,2] Maryse Romao,[2,4] Graça Raposo-Benedetti,[2,4] Bernard S. Lopez,[3] Alain Nicolas,[1,2] Gaël A. Millot[1,2]*

[1] Institut Curie, PSL Research University, CNRS, UMR3244, 26 rue d'Ulm, F-75005, Paris, France

[2] Sorbonne Universités, UPMC Univ Paris 06, CNRS, UMR3244, F-75005, Paris, France

[3] CNRS UMR 8200, Institut de Cancerologie Gustave-Roussy, Université Paris-Saclay, 114 Rue Edouard Vaillant, 94805 Villejuif, France

[4] Institut Curie, PSL Research University, CNRS, UMR144, 26 rue d'Ulm, F-75005, Paris, France

* Corresponding author: gael.millot@curie.fr

Key words

BRCA1, cellular localization, missense mutation, protein misfolding, yeast model

Summary statement

The functional impact of missense mutations (single amino-acid change in a protein) is difficult to predict. Yeast cells detect the misfolding effects of these mutations, occurring in the BRCA1 protein, and uncover an associated nuclear transport impairment.

Abstract

Understanding the effect of an ever-growing number of human variants detected by genome sequencing is a medical challenge. The yeast *Saccharomyces cerevisiae* model has held attention for its capacity to monitor the functional impact of missense mutations found in human genes, including the *BRCA1* breast/ovarian cancer susceptibility gene. When expressed in yeast, the wild-type full-length BRCA1 protein forms a single nuclear aggregate and induces a growth inhibition. Both events are modified by pathogenic mutations of BRCA1. However, the biological interpretation of these events remains to be determined. Here, we show that the BRCA1 nuclear aggregation and the growth inhibition are sensitive to misfolding effects induced by missense mutations. Moreover, misfolding mutations impair the nuclear targeting of BRCA1 in yeast cells and in a human cell line. In conclusion, we establish a connection between misfolding and nuclear transport impairment and we illustrate that yeast is a suitable model to decipher the effect of misfolding mutations.

Introduction

Breast and ovarian cancers are a major health concern, with respectively 1.67 and 0.24 million new cases diagnosed worldwide in 2012 (http://globocan.iarc.fr/). Around 10% of these cases are associated with familial transmission, which frequently involves a germline monoallelic mutation in the *BRCA1* gene (MIM# 113705). This gene encodes a 1,863 amino acid protein that includes two small conserved and structured domains, the RING domain and the BRCT tandem repeats, forming respectively the Nter and Cter extremities of BRCA1, as well as a large central region considered as intrinsically disordered (Mark et al., 2005). Two functional nuclear localization signals (NLSs) and two functional nuclear export sequences (NESs) have also been identified (Chen et al., 1996; Fabbro et al., 2002; Thompson et al., 2005).

Although extensively investigated, the cellular localization and function of BRCA1, as well as its connection with cancer development remains incompletely elucidated. The broadly accepted function of BRCA1 is in the maintenance of the genome through regulation of the DNA double-strand break repair pathway. The nuclear BRCA1 protein participates in DNA repair channeling toward the homologous recombination pathway at the expense of the non-

homologous end-joining pathway during the S and G2/M phases of the cell cycle. This involves the cell-cycle dependent localization of BRCA1 at DNA damage sites (Zimmermann et al., 2013) followed by the recruitment of RAD51 via interaction with PALB2/BRCA2 (Orthwein et al., 2015). Concerning the cellular localization, BRCA1 seems to shuttle between the cytoplasm and the nucleus (Henderson, 2005; Thompson, 2010). The nuclear transport occurs directly, via the internal NLSs of BRCA1, or indirectly, via interaction with BARD1 (Fabbro et al., 2002).

Sequencing the BRCA1 gene uncovered numerous allelic variations. In the BRCA Share database (http://www.umd.be/BRCA1/), 2020 different DNA variants are recorded to date. Among them, missense mutations that result in a single amino acid change, are the most represented with 616 different records (31%). Genetic/epidemiological methods allowed the classification of 20% of them (124/616), either as pathogenic (39/124) or as neutral (85/124), meaning that the medical status of the remaining 498 missense variants is currently unknown. Such lack of information complicates the clinical decision-making after genetic testing of patients and their relatives.

Recently, we proposed to evaluate the pathogenic relevance of BRCA1 missense variants using the yeast *Saccharomyces cerevisiae* model organism, through four different assays: the Colony Size, Liquid Medium, Spot Formation and Yeast Localization assays (Millot et al., 2011; Thouvenot et al., 2016). The Colony Size and Liquid Medium assays monitor the growth inhibition of yeast cells expressing the full length wild type (WT) BRCA1 protein, either by plating the cells on agarose medium and measuring the number of cells in the formed colonies (Colony Size assay), or by monitoring the concentration of cells grown in liquid medium (Liquid Medium assay). In these assays, pathogenic mutations, formally classified by genetic/epidemiological methods, have a tendency to alleviate the growth inhibition observed with the WT BRCA1 protein. The Spot Formation and Yeast Localization assays rely on the observation that the BRCA1-mCherry fusion protein accumulates in a single aggregate inside the nucleus of yeast cells. This aggregate is referred to as "spot" due to its visual signature using fluorescent microscopy. Pathogenic missense mutations decrease the proportion of cells showing one fluorescent spot (Spot Formation assay) and increase the delocalization of BRCA1 nuclear aggregation into the cytoplasm (Yeast Localization assay). Assessment of BRCA1 missense variants in yeast offers three advantages: (1) rapid, large-scale and cost-effective variant classification, (2) evaluation of

variants located in both the Nter and Cter part of the protein and (3) variant classification accuracy up to 92.5%, estimated for the Colony Size assay (Thouvenot et al., 2016). The statistical validation of functional assays is a determinant step for clinical inclusion, which has been completed for these four yeast assays (Thouvenot et al., 2016). However, little is known about their biological relevance. In other words, the reason why pathogenic mutations modify the formation of fluorescent spots and the growth inhibition remains to be elucidated. Here, we provide evidence that both formation of fluorescent spots and growth inhibition are sensitive to the misfolding effects of pathogenic mutations. In addition, we show that misfolding impairs the transport of BRCA1 into the nucleus of yeast and human cells. Finally, we decipher several aspects of the growth inhibition induced by the expression of BRCA1 in yeast.

Results

The human BRCA1 protein aggregates in yeast cells

In a previous study, we speculated that the full-length BRCA1-mCherry fluorescent spot is a protein aggregate, excluded from the nucleolus, and presumably amorphous rather than amyloid like, as it is sensitive to sodium dodecyl sulfate and to sarkosyl (Millot et al., 2011). To confirm that the fluorescent spot visualized in microscopy is an aggregate, we analyzed the organization of large nuclear structures. We show that the nuclear localization of proteasomal proteins is disturbed by the BRCA1-mCherry aggregate. As observed with fluorescent microscopy, the fluorescent signal of Pre6-GFP, a component of the 20S catalytic core of the 26S proteasome, was irregular while homogeneous in absence of BRCA1-mCherry (**Fig. 1A-D**). Pre6-GFP appeared excluded from the aggregate and tended to accumulate around the structure, which resulted in a "hole" pattern in fluorescent microscopy. The same was observed with Pre9-GFP, another component of the 20S core of the proteasome (**Fig. S1**). The genomic DNA is also excluded from the aggregate (**Fig. 1E-F**). Interestingly, while BRCA1-mCherry aggregation fills up to one-third of the volume of the nucleus, this does not affect the localization of 50-100 kDa nuclear proteins. Nab2-GFP and Rat1-GFP exhibited a diffusive signal in fluorescent microscopy, with a similar intensity inside and outside the aggregate (**Fig. S1**). Even the large Rpo21-GFP protein, weighing 191 kDa, was not affected by the BRCA1-mCherry accumulation, suggesting that only very large structures, like the nucleolus, the proteasome and the genomic DNA, are excluded from the amorphous nuclear aggregate.

Next, we benefited from the Pre6-GFP exclusion to determine whether the untagged BRCA1 protein also aggregates in yeast, with the advantage of monitoring living cells, which prevents any potential artifact stemming from cell fixation and anti-BRCA1 antibody labeling. Strikingly, the "hole" pattern was clearly seen in Pre6-GFP cells expressing BRCA1 (**Fig. 1A-D**). Thus, aggregation of BRCA1-mCherry is not caused by the mCherry fusion protein.

We also recovered additional evidence that the BRCA1-mCherry fluorescent spot is an aggregate. Aggregation occurs when the quality-control network of the cell is overwhelmed. This quality-control system is involved in protein homeostasis. With the contribution of molecular chaperones, it facilitates the folding or refolding of misfolded protein species and regulates protein aggregation and degradation (Tyedmers et al., 2010). Here, we show that the double-deletion of the yeast chaperones *ssa1* and *ssa2* decreased the number of cells with fluorescent spots (**Fig. S2A-B**), as well as overexpression of Hsp26 (**Fig. S2C-D**). However, the Hsp104 protein chaperone had no clear influence on the aggregate formation (**Fig. S2E-G**). We also tested the potential involvement of the proteolytic degradation pathways. Deletions of either *ATG8* or *ATG1*, which impair the autophagy pathway (Kraft et al., 2012), had no consequence on the formation of fluorescent spots (**Fig. S3A-D**). Interestingly, inactivation of the proteasome by the deletion of *UMP1* (Ramos et al., 1998) significantly raised the number of cells with fluorescent spots (**Fig. S3E-F**). The number of cells showing two spots was increased four fold in *ump1Δ* cells compared to WT cells. Altogether, these results confirm that the fluorescent spot visualized in microscopy is an aggregate.

The BRCA1 NLS is required for nuclear localization of BRCA1 aggregation

We next investigated if the two endogenous NLSs present in the BRCA1 sequence were necessary for the nuclear localization of the protein in yeast cells. The two NLSs were inactivated by introducing four missense mutations in each sequence (NLSm-mCherry), as previously described (Fabbro et al., 2002). Compared to BRCA1-mCherry, yeast cells expressing NLSm-mCherry exhibited a decrease of cells harboring one spot and an increase of cells with two spots in fluorescent microscopy (**Fig. 2A-B**). Strikingly, fluorescent spots were systematically detected in the cytoplasm and never in the nucleus (**Fig. 2A,C**). This indicates that at least one of the two endogenous NLSs of BRCA1 is functional in yeast. It also confirms our previous results, using the deficient nucleoporin Nup49-GFP construct, that an active transport of BRCA1-mCherry from the cytoplasm toward the nucleus is necessary

for nuclear aggregation (Millot et al., 2011). NLS inactivation completely impairs this mechanism, resulting in cytoplasmic aggregation.

The cytoplasmic aggregation of BRCA1 is distinct from the nuclear aggregation

The GFP-tagged Hsp104 chaperone is known to accumulate around amyloid-prone cytoplasmic aggregates (Kaganovich et al., 2008). Here, Hsp104-GFP colocalized with cytoplasmic but not nuclear aggregates (**Fig. S4A**). The same was observed with the Ssa1-GFP chaperone protein (**Fig. S4B**), with a particularly strong accumulation around NLSm-mCherry cytoplasmic aggregates. In correlative light-electron microscopy (CLEM), the nuclear BRCA1-mCherry spot, visualized in fluorescence, was undetectable in electron microscopy (**Fig. S4C**). However, the cytoplasmic NLSm-mCherry spot appeared as a large structure, devoid of membrane and excluding the ribosomal granulations that darken the cytoplasm (**Fig. S4D**). Altogether, these results support a BRCA1 amorphous aggregation in yeast cells, with a nuclear localization of this event that depends on BRCA1 functional NLSs.

Misfolding hampers the nuclear aggregation of BRCA1 in yeast cells

Next, we examined whether the conformation of the BRCA1 protein is important for the formation of fluorescent spots. According to the literature (Williams et al., 2003; Lee et al., 2010), we selected four missense mutations that strongly destabilize the structure of the BRCT domain (T1691K, G1706E, R1751P and W1837C) and four missense mutations that exhibit minor effects (R1699W, R1751Q, V1804D and P1859R). The three mutations T1691K, G1706E and W1837C induced a strong decrease of cells harboring fluorescent spots compared to WT BRCA1 (**Figs. 3A-B** and **3F**, left panel). The same result, but to a lesser extent, was observed with R1751P, whereas negative controls exhibited no effects. Thus, misfolding of BRCA1 impairs the the formation of fluorescent spots. We confirmed this result using data from 18 additional BRCA1 missense mutations, located in the BRCT domain (**Fig. S5C** and **Table S2**). From this, we conclude, first, that yeast cells are able to detect misfolding of the heterologous BRCA1 protein, and second, that the formation of fluorescent spots is an effective readout of misfolding events. Strikingly, the three mutations T1691K, G1706E and W1837C induced a complete delocalization of the spots into the cytoplasm compared to WT BRCA1 (**Figs. 3C** and **S6A**). Again, the same result, but to a lesser extent, was observed with R1751P. Thus, the misfolding of the BRCT domain prevents the BRCA1 protein transport into the nucleus. Altogether, these results show that the spot formation and delocalization are efficient reporters of BRCA1 misfolding. In addition,

pathogenic mutations R1699W, M1775K and M1775R poorly disturb the structure of BRCA1, and poorly affect the formation of fluorescent spots in the nucleus or the delocalization (**Fig. S5C-D**), which indicates that yeast cells do not reveal the pathogenicity of the mutations *per se* but the misfolding effect of missense mutations.

Misfolding hampers the nuclear localization of BRCA1 in human cells

To determine whether the delocalizing effect of misfolding mutations is restricted to yeast cells, we introduced the 8 mutations in a mCherry-BRCA1 expression vector specific to human cells and evaluated the effect of these mutations in human SV40 transformed fibroblast RG37 cells. The cytoplasmic localization of BRCA1 was clearly increased with the 4 misfolding mutations but not with the 4 controls (**Figs. 3D**, **S6B** and **S7**), indicating that misfolding impairs the transport of BRCA1 toward the nucleus. Correlation between results obtained in human and yeast cells reached 0.97 (**Fig. 3E**). This shows that the spot formation and delocalization in yeast cells is an effective readout of results obtained either *in vitro*, concerning BRCA1 misfolding, or in human cells concerning BRCA1 nuclear transport defects.

The RING and BRCT domains are not required for BRCA1 aggregation in yeast

We next wondered if the two large structured domains of BRCA1, namely the RING and BRCT domains, located at each extremity of the protein, were involved in the nuclear aggregation observed in yeast cells. Surprisingly, truncation of both extremities of BRCA1 had no impact on the formation of fluorescent spots when compared to the full-length protein **(Fig. 4**, Central construction**)**. This indicated that the intrinsically disordered central part alone is sufficient to promote BRCA1 aggregation in yeast. In contrast, truncation of the intrinsically disordered central part of BRCA1 (Nter-Cter construction) fully impaired the formation of fluorescent spots in the nucleus (**Fig. 4**). Instead of a signal restricted to a subdomain of the nucleus, a diffuse signal was visualized filling both the nuclear and cytoplasmic cell compartments, with occasionally an additional small fluorescent spot in the cytoplasm. Altogether, we conclude that the structured domains do not contribute to BRCA1 aggregation. Using the Nter-Cter construction, keeping the first endogenous NLS of BRCA1 (Nter-NLS-Cter construction), the signal visualized in fluorescent microscopy systematically filled the entire nucleus, which is the feature of diffusive nuclear proteins. This confirms that the first endogenous NLS of BRCA1, at least, is operational in yeast. This also shows that the

RING or the BRCT domain does not promote aggregation in yeast, even when located in the nucleus.

Misfolding induces cytoplasmic delocalization in the absence of aggregation

How can we reconcile the fact that structured domains are not involved in the formation of fluorescent spots and that misfolding mutations in the structured domains impair this spot formation? To answer this question, we integrated misfolding mutations in the Nter-NLS-Cter construction (**Fig. 5A**). The Y1853X nonsense mutation results in the loss of the ten last amino acids of BRCA1, which destabilizes the BRCT structure (Williams et al., 2001) and delocalizes the full-length BRCA1 aggregation into the cytoplasm in yeast cells (Millot et al., 2011). Strikingly, both W1837C and Y1853X mutations strongly impaired the nuclear localization of the Nter-NLS-Cter peptide (**Fig. 5B-C**). Thus, mutations that delocalize the BRCA1 aggregation into the cytoplasm delocalize the Nter-NLS-Cter peptide in the same manner. This demonstrates that the nuclear aggregation of BRCA1 and the delocalization triggered by misfolding mutations are two distinct events. From this, we conclude that yeast cells are able to detect misfolding of synthetic peptides, independently of any aggregation mechanism.

Nuclear aggregation is not sufficient to fully explain the growth inhibition induced by WT BRCA1 expression

It has been known for a long time that expression of the full-length human BRCA1 protein in yeast cells compromises cell growth (Humphrey et al., 1997; Caligo et al., 2009; Millot et al., 2011). However, the origin of this growth inhibition is poorly understood. Here, we show a connection between nuclear aggregation and growth inhibition. Compared to the WT BRCA1 protein, cell growth was recovered with NLSm (**Fig. 6A**) and with mutations that misfold the BRCT domain (**Fig. 6B**). Strikingly, expression of the intrinsically disordered central part of BRCA1 alone was sufficient to promote a growth inhibition comparable to that in cells expressing the full length protein (**Fig. 6C**). Moreover, growth rates negatively correlate with the proportion of cells exhibiting one spot in fluorescent microscopy and correlate with spot delocalization (**Figs. 6D-E** and **S5F-G**). Lastly, just as the proportion of cells showing one fluorescent spot and spot delocalization, growth rates negatively correlate with the structural stability of the protein (**Fig. S5B**,**E**). All of these results point to the connection between nuclear aggregation and growth inhibition, which is also confirmed by the results previously obtained with the defective Nup49 nucleoporin (Millot et al., 2011). This suggests that

aggregation of BRCA1, mediated by its central domain, inhibits cell proliferation when taking place in the nucleus, and events leading to decreases and/or delocalization of aggregation, like misfolding, restore cell growth.

To confirm the connection between nuclear aggregation and growth inhibition at the cellular level, we scrutinized cells using fluorescent videomicroscopy. In a period of 6 hours, 89% of individual cells exhibiting a fluorescent spot did not divide while the proportion was 8% when no spot was detected (**Movie S1** and **Fig. 6F**). Most of the time, the cell cycle arrest occurred in G1 (**Fig. S8A**). Thus, the nuclear aggregation of BRCA1 is frequently associated with a cell cycle arrest in G1. This arrest is independent of Mec1, the yeast homolog of ATR involved in G1/S and S/G2 checkpoints (Sidorova and Breeden, 1997), indicating that the DNA damage response is not activated (**Fig. S9A-B**).

However, a potential cellular toxicity due to visible BRCA1 aggregates, is not sufficient to fully explain the growth inhibition observed. As shown in **Figs. 2B** and **3B**, approximately one third of cells exhibit the nuclear spot after 4 hours of BRCA1-mCherry expression. This means that in long term cultures, cells exhibiting the fluorescent spot and blocked in G1 should be diluted among the cells that do not exhibit the spot and that proliferate. **Fig. S10** confirmed this dilution effect. However, videomicroscopy in transillumination (**Movies S2 and S3**) revealed that the growth inhibition is a combination of cells that grow slowly (compared to vector cells) and cells that are blocked in G1 (**Fig. S8B-E**). Long term cultures on plates and in liquid medium confirmed the absence of cells showing rapid cell-cycles when expressing BRCA1 (**Fig. S8F-G**). Finally, this suggests that the growth rate of cells expressing BRCA1, without visible nuclear aggregation, is also hampered but to a lesser extent than cells exhibiting the nuclear aggregate. Thus, visible nuclear aggregation is not sufficient to fully explain the growth inhibition induced by WT BRCA1 expression.

A strong expression of WT BRCA1 compensates for the high instability of the protein in yeast cells and generates efficient nuclear aggregation and growth inhibition

The plasmid used to express BRCA1 is a 2µ plasmid, widely employed in yeast. The main advantage of 2µ plasmids is the copy number per cell, which can reach 100. However, it is also known to be unstable and copy numbers can strongly vary from cell to cell (Futcher and Cox, 1984). We suspected that cells exhibiting the nuclear fluorescent spot, and blocked in G1, are those that contain a high number of plasmids and thus that express a high level of BRCA1 protein. To verify this, we integrated the *GAL1p-BRCA1* construction as a single copy in the yeast genome. In this configuration, cell proliferation was unaffected (**Fig. 7A**,

right panel). Surprisingly, the BRCA1 protein could not be detected by Western blot analysis (**Fig. 7B**, middle lane), even if the mRNA is transcribed (**Fig. S11**). Experiments using the translational inhibitor cycloheximide (CHX) confirmed the strong instability of the BRCA1 protein in yeast, as compared to the Tubulin protein, with an approximate 2 hour half-life (**Fig. S12A**). Such a high instability is consistent with the pattern of degradation visible in Western blots, below the major band (e.g., **Fig. 7B**, left lane). Proteasomal degradation is, at least in part, responsible for the BRCA1 instability, since the proteasome inhibitor MG132 hampered the decrease of BRCA1 protein levels in cells treated with CHX during four hours (**Fig. S13A**). Interestingly, the fluorescent spot formation was reduced concomitantly with proteins levels in CHX experiments (**Figs. S12E-F** and **S13D-E**). This result supports the requirement of strong BRCA1 expression for efficient aggregation.

We also replaced the *GAL1* promoter (*GAL1p*) on the 2µ plasmid by the constitutive *ADH1* promoter (*ADH1p*). In yeast cells transformed with the *ADH1p-BRCA1* construct, the BRCA1 protein was visible in Western blot analysis (**Fig. 7B**, right lane), but the band intensity indicated that, on average, the protein amount per cell was lower than with the *GAL1* promoter. In addition, the BRCA1-mCherry spot formation was less efficient with the *ADH1* promoter than with the *GAL1* promoter (**Fig. 7C-D**). Lastly, a decrease of proliferation was observed with the *ADH1* promoter, compared to empty Vector cells (**Fig. 7A**, left panel), but the result is less dramatic than the one classically obtained with the *GAL1* promoter (**Fig. 7A**, middle panel).

All these results show that strong expression is necessary for efficient BRCA1 aggregation and growth inhibition. The cellular heterogeneity regarding nuclear aggregation and cell-cycle arrest (**Movie S1**) is probably the consequence of plasmid copy number variation: both events are obtained only within cells carrying a sufficient number of plasmids. From this, we propose that the increasing expression of BRCA1 leads to a graduated phenotype: from no consequence (single *BRCA1* copy inserted), growth slowed down, growth slowed down and nuclear aggregation (rare event in **Movie S1**), up to cell cycle arrest and nuclear aggregation.

High expression levels of BRCA1 and nuclear transport is required for efficient growth inhibition

Do the average levels of BRCA1 protein per cell reflect the need of a strong expression system for efficient BRCA1 aggregation and growth inhibition? As shown by Western blot analyses, variations in protein levels are observed with truncated forms of BRCA1 but the connection with cytoplasmic aggregation and growth inhibition is not evident (**Fig. S14A-C**

and (Millot et al., 2011)). In contrast, the misfolding mutations T1691K, G1706E and W1837C, which induce strong delocalization of aggregation into the cytoplasm, as well as strong cell growth restoration, all exhibited particularly high levels of full-length proteins (**Fig. 3G**). Although the opposite results were expected, this confirms previous results obtained with other missense mutations (Millot et al., 2011; Thouvenot et al., 2016). Interestingly, such results indicate that high protein levels detected in Western blots appear to be an additional signature of misfolding induced by missense mutations. As shown in **Fig. 3H**, right panel, and **Fig. S5I**, such a readout possesses low sensitivity (not all of the misfolding mutations exhibit a high protein level, like R1751P), but 100% specificity (a high protein level supports a missense mutation that generates misfolding events). Intriguingly, the higher levels of mutated BRCA1 protein, when aggregation occurs in the cytoplasm, cannot be explained by better stability of the protein. Indeed, in CHX experiments, the half-life of the full-length BRCA1 protein is similar, with or without the presence of the misfolding mutation T1691K (**Fig. S12A-B**). Moreover, in both cases, the formation of fluorescent spots is strongly affected (**Fig. S12E-H**) and sensitivity to proteasome inhibition is observed (**Fig. S13**). In fact, the higher levels of BRCA1 protein, occurring with cytoplasmic aggregation, could be explained by using the conclusion from the precedent section: strong expression of the WT BRCA1 protein induces a progressive decrease of the proportion of yeast cells carrying a high number of 2µ expression plasmids during liquid culture, due to cell cycle arrest in G1. This diluting effect of cells that contain high levels of BRCA1 proteins would not happen with T1691K, G1706E or W1837C, as cell growth is much less inhibited. This explanation is supported by the analysis of the complete lanes in Western blots (blue numbers in **Fig. S12A-C**), since the level of peptide is increased 2.94 times between two hours and six hours of galactose induction with the T1691K misfolding mutation, while this level is stable with the WT BRCA1 protein and the R1751Q control mutation.

From these results, we conclude that a high protein level, observed by Western blots, is a signature of misfolding for certain BRCA1 missense mutations, but that the level of full-length BRCA1 protein *per se* is not the sole determining factor of growth inhibition. In fact, a critical point provided by this study seems to be the level of BRCA1 protein transported into the nucleus. Impairment of this transport through endogenous NLS mutations (**Fig. 2**), Nup49 defect (Millot et al., 2011) or misfolding (**Figs. 3** and **S5**), as shown by the resulting cytoplasmic aggregation, alleviate the growth inhibition (**Fig. 6**).

Altogether, these results allow us to propose a model regarding the expression of the full-length BRCA1 protein in yeast cells (**Fig. 8**): after synthesis in the cytoplasm, the protein is

transported into the nucleus, using at least one endogenous NLS, where a high protein concentration triggers amorphous aggregation, via the intrinsically disordered central part of BRCA1, as well as a growth inhibition. Reducing the protein concentration in the nucleus diminishes both nuclear aggregation and growth inhibition. This reduction may have different origins, including misfoldings that occur in structured domains of BRCA1, which hinder nuclear transport.

Discussion

In this work we show that yeast cells detect misfolding of the full-length human BRCA1 protein. We illustrated this using a total of 14 missense mutations known to misfold the BRCT domain (4 mutations in **Fig. 3** and 10 more in **Fig. S5C-E**), but the results are also corroborated with truncations. Indeed, the complete truncation of the RING domain (Millot et al., 2011), BRCT domain (Millot et al., 2011), or both (**Figs. 4,6**) do not affect the nuclear spot formation and growth inhibition, contrary to internal truncations in these domains (Millot et al., 2011). This suggests that the conformational state of these domains is essential to the formation of the nuclear spot and the growth inhibition.

We also show that misfolding mutations hamper the nuclear transport of BRCA1 in yeast cells and in the human RG37 cell line. These results consolidate previous results about BRCA1 delocalization obtained in other human cell lines, using missense or truncating mutations (Rodriguez et al., 2004), suggesting a connection between the protein structural stability and a nuclear transport clearance. In tumoral or normal cells from patients with BRCA1 germline mutations, contradictory results were reported, like cytoplasmic (Perez-Valles et al., 2001), diffusive (Tulchin et al., 2013) or absence of signal (De Brakeleer et al., 2007), probably because of variations in the sensitivity and specificity of the anti-BRCA1 antibodies used and lack of robust results when repeating BRCA1 immunohistological staining experiments (Wilson et al., 1999; Milner et al., 2013). Thus, no sound confirmation or refutation can be currently drawn from the delocalization effect of misfolding mutations using these kinds of experiments.

This study uncovers yeast as a simple and rapid model to assess the structural stability of BRCA1 mutations. The fact that yeast cells detect the misfolding of the Nter-NLS-Cter peptide (**Fig. 5**) has also interesting prospects in functional assessment of mutations. Indeed,

this means that the delocalization events of BRCA1 triggered by misfolding could be effective for other human nuclear proteins that do not necessarily aggregate in yeast. Such yeast assay, based on the nucleo-cytoplasmic delocalization readout, could be easily derived from the system presented here, the limitation being the length of the peptide analyzed (40-50 kDa minimum) to prevent a passive nucleo-cytoplasmic diffusion through the nuclear membrane (Shulga et al., 2000).

In a previous study, we estimated the clinical relevance of four different yeast assays (Colony Size, Liquid Medium, Spot Formation and Yeast Localization assays), based on the formation of fluorescent spots, spot localization or growth inhibition readouts, in the classification of BRCA1 missense variants (Thouvenot et al., 2016). Here, we show that misfolding detection is an important component of the readouts of these four assays, as shown by the correlation values obtained (**Figs. 3F** and **S5B-E**). This has several consequences regarding the use of yeast cells to classify BRCA1 variants. First, the fact that the four yeast functional assays are adapted to the assessment of missense mutations located in the RING domain of BRCA1 (Thouvenot et al., 2016), suggests that yeast cells are able to detect misfolding taking place in this domain. Second, we predict that the four functional assays are poorly adapted to missense mutations located in the large intrinsically disordered central part of BRCA1 (1,500 amino acid sequence between the RING and the BRCT domains). Third, the four BRCA1 functional assays could be considered as misfolding more than pathogenic indicators. This means that these yeast assays could also be used as complementary assays, to decipher the deleterious effects of variants previously classified as pathogenic by genetic/epidemiological methods or by other functional assays. Finally, other unidentified phenomena, other than misfolding, could also be part of the readouts of the four assays, which would explain the few discrepancies observed between the assay results (Thouvenot et al., 2016).

The toxicity induced by expression of the full-length BRCA1 in yeast has long been a mystery (Humphrey et al., 1997). With the concordance between BRCA1 nuclear aggregation and growth inhibition, systematically and concomitantly hampered by mutations, truncations or nucleoporin defects (this study and (Millot et al., 2011; Thouvenot et al., 2016)), it is tempting to consider a direct contribution of the BRCA1 nuclear aggregate to this toxicity. However, we provide evidence, here, that the growth rate of cells expressing BRCA1, without visible nuclear aggregation, is also hampered but to a lesser extent than cells exhibiting the nuclear aggregate. Thus, it seems likely that nuclear aggregation merely

reflects intranuclear BRCA1 concentrations, and that the toxicity is due to a soluble fraction of the complete form of the BRCA1 protein, or of a fragment from degradation. Importantly, we show that the level of BRCA1 protein is a determinant factor of toxicity, provided that these proteins are transported into the nucleus. The endogenous NLSs of BRCA1 are required for the transport. However, the fact that the deficient Nup49 alleviates the growth inhibition (Millot et al., 2011) may be an indication that the toxicity is not the consequence of importin titration by these NLSs. Bennett et al proposed that the toxicity results from a Spt4-dependent BRCA1 interaction with the yeast RNA polymerase II, inducing a protease activity that cleaves this polymerase (Bennett et al., 2008). We cannot exclude an effect of the nuclear Spt4 protein in the BRCA1 toxicity, which would corroborate the importance of the BRCA1 localization in the nucleus, but we were unable to confirm the RNA pol II cleavage in Western blot experiments (**Fig. S14D**). However, contrary to previous statements (Humphrey et al., 1997; Bennett et al., 2008; Couch et al., 2008), we prove here that the toxicity induced by the full-length BRCA1 is not mediated by the BRCT domain. This indicates that the toxicity resulting from the full-length BRCA1 protein and from small synthetic NLS-BRCT constructs (Humphrey et al., 1997; Coyne et al., 2004) have distinct origins. Lastly, we suspect that the concordance between BRCA1 nuclear aggregation and growth inhibition depends on a specific interaction between the *GAL1* promoter and the 2µ plasmid used. Indeed, in long term cultures, the nuclear aggregate is hardly seen using the *GAL1* promoter (**Fig. S10**), while 10% of the cells exhibit the nuclear aggregate with the *ADH1* promoter (**Fig. 7D**). Further investigation will be required to completely decipher the toxicity induced by the full-length BRCA1 protein in yeast cells, but we show here that the *GAL1* promoter - 2µ strategy used in the BRCA1 functional assays is the most efficient in term of formation of fluorescent spots and growth inhibition.

Finally, this study highlights the BRCA1 expression in yeast as an interesting model of nuclear aggregation, a phenomenon less investigated than cytoplasmic aggregation. We previously reported that the BRCA1 aggregation was amorphous and microtubule dependent (Millot et al., 2011). Here we show that the cytoplasmic chaperones Ssa1, Ssa2 and Hsp26 are involved in the regulation of this process, suggesting that the nuclear aggregation is, at least in part, controlled in the cytoplasm. Importantly, we believe that our model is adapted to high-throughput screening of chemical compounds that misfold BRCA1, or that would refold mutated forms of BRCA1, similar for instance to the effect of the NSC319726 molecule on the R175H mutated allele of p53 (Yu et al., 2012). Lastly, recent studies reported that

chaperone proteins may provide a capacitor effect, which is defined by an ability to mask deleterious effects of mutations that are released when capacitors are absent (Rutherford and Lindquist, 1998; Jarosz and Lindquist, 2010). Since most of the pathogenic missense mutations seems to misfold BRCA1 (Lee et al., 2010), we suspect that the misfolding effect of missense mutations could be a key component of this capacitor effect. This could explain the low penetrance observed for some missense mutation-dependent genetic diseases, which would be related to individual variations in chaperone levels. Again, the model of BRCA1 expression in yeast could be adapted to such investigations.

Materials and Methods

Plasmids

Plasmids are listed in **Table S3**. Except for the 12 last plasmids of this table, all of the plasmids are derived from pJL45 and pGM40, a modified version of pESC-URA containing the human full-length BRCA1 cDNA (Millot et al., 2011). In these plasmids, expression of the cDNA is controlled by the *GAL1* promoter, inducible by galactose and repressed by glucose, except for pGM35, pGM36 and pGM96, for which the *GAL1* promoter has been replaced by the constitutive *ADH1* promoter. Missense mutations were generated as in (Thouvenot et al., 2016). The two BRCA1 NLSs were replaced by a cassette incorporating the mutated NLSs and coming from the pFlag-BRCA1-NLSm plasmid (gift from Henderson). Deletions in the 5' or 3' BRCA1 cDNA sequence were produced by standard PCR. In the Nter-NLS-Cter Δ(101-494; 517-1639) construct, the first deletion was replaced by a Ser-9Gly-Ser-2Gly-2Ser linker, and the second deletion by a Gly-2Ser-10Gly linker. In the Nter-Cter Δ(101-1639) construct, the deletion was replaced by a Ser-9Gly-Ser-2Gly-2Ser-10Gly linker. In the yeast mCherry fusion constructs, the mCherry DNA sequence (GenBank: AY678264.1) was separated from the 3' end cDNA by a 10Gly linker. The human expression plasmids (pGM137, pGM140 and pBB9 to pBB16) are derived from the pEGFP-C1 plasmid, in which the *GFP* sequence was replaced by *BRCA1* sequences, using the AgeI/SmaI digestion. The mCherry sequence was separated from the 5' *BRCA1* cDNA by a 10Gly-Lys-Leu-Thr linker. The inserted sequences are under the control of the Cytomegalovirus (CMV) promoter. The pGM35, pGM36 and pGM96 plasmids were obtained by replacing the *GAL1* promoter of the pJL48, pJL45 and pGM40 respectively, by the *ADH1* promoter. The pJL62 and pJL59 are derived from the pRS304 plasmid (Sikorski and Hieter, 1989).

Yeast strains

Cells listed in **Table S4** were treated as in (Millot et al., 2011).To check that the coding sequence was correctly deleted in the genome (Winzeler et al., 1999) or that the coding sequence was correctly fused to the GFP sequence (Huh et al., 2003), a PCR using two primers flanking the integration area was performed on the genomic DNA, and the PCR product was sequenced. Promoters of the *HSP26* and *HSP104* genes were replaced by the *GPD* promoter using the pYM-N14 and pYM-N15 plasmids, according to Janke et al (Janke et al., 2004). The *ssa1Δssa2Δ* strain was built according to (Winzeler et al., 1999). BRCA1 constructs were integrated in the yeast genome at the *TRP1* locus, after digestion of pJL59 and pJL62 by EcoRV. In experiments using galactose induction, cells were grown in glycerol lactacte medium (GL), which allows a rapid BRCA1 expression (30 min as shown in **Fig. S10D**).

Cell culture

Growth inhibition was monitored in liquid medium as described in Thouvenot et al (Thouvenot et al., 2016). Briefly, cells were prestimulated in galactose or glucose for 7 hours, were resuspended at 10^6 or 0.5×10^6 cells/ml, respectively, and were grown for another 15 hours. Cell concentration was then measured by optical density at 600 nm (1 OD600 corresponding to 1.15×10^8 cells/ml). For experiments involving the *ADH1* promoter, cultures were performed using DO-URA instead of GL-URA medium (Millot et al., 2011). Of note, contrary to microscopy experiments, the proteins expressed in cell growth experiments are not fused to mCherry, for two reasons: first, these kinds of constructions are used in the Colony Size and Liquid Medium assays (Thouvenot et al., 2016) and second, cell growth results are globally similar with or without the mCherry fusion (correlation of 0.96, as shown in (Millot et al., 2011)). For fluorescent microscopy analyses, cells were induced for 4 hours with galactose, unless otherwise specified. In Hsp104 inhibition experiments (Ferreira et al., 2001), cells were grown for three days in GL-URA medium (Millot et al., 2011) supplemented with 5mM guanidine hydrochloride. Dilution of the culture was performed twice per day to prevent cell growth saturation. Then, galactose was added and fluorescent microscopy analyses were performed four hours later.

Transfection of human cells and irradiation

RG37 cells are SV40-transformed human fibroblasts (Dumay et al., 2006). Cells were cultured in Dulbecco's modified Eagle's medium supplemented with 10% fetal calf serum, 2 mM glutamine, and 200 IU/ml penicillin, and incubated at 37°C under 5% CO2. Thawed batches were tested for contamination prior use. Cells were plated 24 hours prior to mCherry-BRCA1 transient transfection (JetPEI, Polyplus, Ozyme). For irradiation, cells were exposed to 10 Gy ionizing radiation 24h after transfection using a 137Cs source (2,8 Gy/min) and a IBL-637 (CIS-BioINternational) gamma irradiator (662 keV photons).

Microscopy of human cells

Cells were grown on glass coverslips. Twenty four hours after transfection, or 4h or 7h after irradiation, the cells were washed in PBS and fixed in 4% paraformaldehyde 15min at room temperature (RT). The cells were then incubated with PBS containing 1% Triton X-100 for 5min at RT. After blocking in PBS containing 2% BSA and 0.05% Tween-20 solution for 30min at RT, immunostaining was performed using the rabbit anti-mCherry (Institut Curie, APR#13, 1:250 dilution) primary antibody for 1h30 at RT with antibodies diluted in PBS containing 1% BSA and 0.05% Tween-20. Of note, we by-passed the BRCA1 antibody concerns regarding artifactual BRCA1 localizations (Wilson et al., 1999), using mCherry-BRCA1 constructs and the mCherry antibody. Next, the coverslips were incubated for 45 min with Alexa 568-conjugated anti-rabbit secondary antibodies (Life technologies) at RT and mounted in mounting medium (Dako) supplemented with DAPI (4',6-diamidino-2-phenylindole). Images were captured using a Zeiss Axio Imager Z1 microscope with a 30x objective equipped with a Hamamatsu camera. Acquisition was performed using AxioVision (4.7.2.). Images were analyzed using the ImageJ software.

Microscopy of yeast cells

Live fluorescent microscopy analyses were performed as previously described (Millot et al., 2011). Unless otherwise specified, cells were induced for 4 hours with galactose before microscopy analysis. For each field (images or movies), the final GFP and mCherry pictures obtained were inverted maximum projections of 16 acquisitions along the z-axis, every 300 nm. The number of cells analyzed is shown in **Table S1**. Cells were confluent during the period of live picture acquisition to increase the number of cells per field and thus to increase the statistical power of picture analysis. The cytoplasmic delocalization of the fluorescent

spot was evaluated as previously described (Thouvenot et al., 2016), except that images were not deconvoluted (segmentation of the spots improved). In protein stability experiments, the final concentration of cycloheximide, diluted in ethanol 100%, was 200 µg/ml (**Figs. S12** and **S13**). The final concentration of MG132, diluted in pure Dimethyl sulfoxide (DMSO), was 100 µM (**Fig. S13**).

The nuclear DNA exclusion in living cells (**Fig. 1E**) was observed following the method of Koszul et al (Koszul et al., 2009). Briefly, Nup133-GFP cells expressing BRCA1-mCherry were incubated overnight at 4°C in the medium culture, supplemented with 20 µg/ml DAPI, before direct analysis. The montage represented in **Fig. 1E** is a single slice from 22 deconvoluted acquisitions along the z-axis every 200 nm.

Analysis of fixed cells (**Fig. 1F**) was carried out as follows. Wild type (WT) yeast cells expressing BRCA1-GFP were induced for 4 hours with galactose. Next, cells were resuspended at 200,000 cells/ml in freshly made fixation buffer (20 mM KPO4 pH6.4, 4% formaldehyde) for 1 hour at room temperature (RT). Cells were washed twice with 0.1 M KPO4 and incubated 3 minutes in 100 mM Tris-HCl pH9.4, 10 mM dithiothreitol (DTT). Next, cells were washed in sphero-buffer (100 mM KPO4, 1.2 M Sorbitol) and converted into spheroplasts using sphero-buffer + 0.2 mg/ml Zymolyase 100T for 10 minutes at 30°C. Spheroplasts were fixed on poly-L-Lysine coated coverslips and incubated in 1X PBS, 0.1% triton X-100 for 10 minutes, washed in 1X PBS, incubated in 1 µg/ml DAPI for 5 minutes, washed in 1X PBS and finally mounted for fluorescent microscopy. The montage represented in **Fig. 1F** is an inverted maximum projection of 16 deconvoluted acquisitions along the z-axis every 200 nm.

Correlative light-electron microscopy (CLEM)

The method is described in Heiligenstein et al (Heiligenstein et al., 2014). Briefly, cells expressing BRCA1-mCherry or NLS-mCherry were induced for 4 hours with galactose. Then, cells were vitrified by high pressure freezing and embedded in HM20 Lowicryl resin to preserve the mCherry fluorescence in the sample. Semi-thin sections (100nm) were collected on an electron microscopy (EM) grid and fluorescent pictures were taken using a 60x oil immersion epifluorescence microscope. Fluorescence images were denoised and flattened using the eC-CLEM software. The sections were then contrasted for electron microscopy (Reynolds lead citrate and Uranyl acetate) and electron micrographs of the target cells were acquired. Fluorescent pictures were overlayed onto the EM micrographs using eC-CLEM.

Western blot

Western blots were performed as previously described (Millot et al., 2011). Unless otherwise specified, cells were induced for 4 hours with galactose before cell lysis and total protein analysis. We showed that the mCherry fusion has little impact on Western blot results (Thouvenot et al., 2016). Thus, lysates from cells expressing BRCA1 fused to mCherry were sometimes used in Western blot analyses: (1) when the anti-BRCA1 antibody epitope was not present (i.e., constructions depicted in **Fig. S14B-C**) and (2) in **Figs. S12** and **S13**. The primary antibodies used were mouse anti-BRCA1 (MS110, Calbiochem, Billerica, MA, USA, ref OP92, 1:200 dilution), rat anti-Tubulin (YL1/2, AbD serotec, Oxford, UK, ref MCA77G, 1:2,000 dilution), rabbit anti-mCherry (Institut Curie, APR#13, 1:1,200 dilution), goat anti-Rad53 (YC19, Santa Cruz Biotech, Dallas, TX, USA, ref SC-6749, 1:600 dilution) and mouse anti-RNA pol II (8WG16, Covance, Emeryville, CA, USA, ref MMS-126R, batch E10015AF, 1:500 dilution). The secondary peroxidase-conjugated antibodies were anti-mouse (Jackson Immunoresearch, West Grove, PA, USA, ref 115-035-146, 1:10,000 dilution), anti-rat, anti-rabbit (Jackson Immunoresearch, ref 112-035-062, ref 711-035-152, ref 1:5,000 dilution) and and anti-goat antibodies (Promega, Madison, WI, USA, ref V0851, 1:5,000 dilution). The ImageJ software was used to quantify signal intensities.

Statistical analysis

Statistical analyses were performed as previously described (Millot et al., 2011). Results are summarized in **Table S1**. A total of three independent clones were analyzed if a significant difference was obtained using the first clone.

Acknowledgments

The authors would like to sincerely thank Beric R. Henderson for the pFlag-BRCA1-NLSm plasmid (Fabbro et al., 2002), Anne Peyroche and Benoît Le Tallec for the BLT67 strain (Le Tallec et al., 2007), Michel Toledano for the Hsp104-GFP strain, Allyson Holmes and Benoît Le Tallec for critical reading of the manuscript, Angela Taddei's team, Frank Perez, Sophie Loeillet, Marc Lecuit, Thomas Boudier, Judith Lopes, Lélia Soter, Patricia Le Baccon, Jean-Baptiste Sibarita, Vincent Fraisier, Lucie Sengmanivong, the Nikon Imaging Center and the PICT-IBiSA imaging facility for technical assistance.

Competing interests

No competing interests declared.

Author contributions

Conception and design: G.A. Millot
Development of experimental methodologies: G.A. Millot, P. Thouvenot, V. Lejour, E. Dardillac, B.S. Lopez, X. Heiligenstein, G. Raposo-Benedetti, A. Nicolas
Acquisition of data: P. Thouvenot, G.A. Millot, L. Fourrière, E. Dardillac, B. Ben Yamin, A. Lescure, J.B. Boulé, X. Heiligenstein, M. Romao
Writing, review and revision of the manuscript: G.A. Millot, X. Heiligenstein, B.S. Lopez, J.B. Boulé
Study supervision: G.A. Millot

Funding

This work was supported by Fondation ARC pour la Recherche sur le Cancer [PJA 2013 1200463 to G.A.M.]; and Institut Curie [CEST 2011 95011, 2012 95023, 2013 95030 to G.A.M. and PIC "Cellular models and Clinical Scenario" 2013 91920 to G.A.M.].

References

Bennett, C. B., Westmoreland, T. J., Verrier, C. S., Blanchette, C. A., Sabin, T. L., Phatnani, H. P., Mishina, Y. V., Huper, G., Selim, A. L., Madison, E. R. et al. (2008). Yeast screens identify the RNA polymerase II CTD and SPT5 as relevant targets of BRCA1 interaction. *PLoS ONE* **3**, e1448.

Berens, T. J. and Toczyski, D. P. (2012). Colocalization of Mec1 and Mrc1 is sufficient for Rad53 phosphorylation in vivo. *Mol Biol Cell* **23**, 1058-67.

Caligo, M. A., Bonatti, F., Guidugli, L., Aretini, P. and Galli, A. (2009). A yeast recombination assay to characterize human BRCA1 missense variants of unknown pathological significance. *Hum Mutat* **30**, 123-33.

Chen, C. F., Li, S., Chen, Y., Chen, P. L., Sharp, Z. D. and Lee, W. H. (1996). The nuclear localization sequences of the BRCA1 protein interact with the importin-alpha subunit of the nuclear transport signal receptor. *J Biol Chem* **271**, 32863-8.

Couch, F. J., Rasmussen, L. J., Hofstra, R., Monteiro, A. N., Greenblatt, M. S., de Wind, N. and Group, I. U. G. V. W. (2008). Assessment of functional effects of unclassified genetic variants. *Hum Mutat* **29**, 1314-26.

Coyne, R. S., McDonald, H. B., Edgemon, K. and Brody, L. C. (2004). Functional Characterization of BRCA1 Sequence Variants Using a Yeast Small Colony Phenotype Assay. *Cancer Biol Ther* **3**, 453-7.

De Brakeleer, S., Bogdani, M., De Greve, J., Decock, J., Sermijn, E., Bonduelle, M., Goelen, G. and Teugels, E. (2007). Loss of nuclear BRCA1 protein staining in normal tissue cells derived from BRCA1 and BRCA2 mutation carriers. *Mutat Res* **619**, 104-12.

Dumay, A., Laulier, C., Bertrand, P., Saintigny, Y., Lebrun, F., Vayssiere, J. L. and Lopez, B. S. (2006). Bax and Bid, two proapoptotic Bcl-2 family members, inhibit homologous recombination, independently of apoptosis regulation. *Oncogene* **25**, 3196-205.

Fabbro, M., Rodriguez, J. A., Baer, R. and Henderson, B. R. (2002). BARD1 induces BRCA1 intranuclear foci formation by increasing RING-dependent BRCA1 nuclear import and inhibiting BRCA1 nuclear export. *J Biol Chem* **277**, 21315-24.

Ferreira, P. C., Ness, F., Edwards, S. R., Cox, B. S. and Tuite, M. F. (2001). The elimination of the yeast [PSI+] prion by guanidine hydrochloride is the result of Hsp104 inactivation. *Mol Microbiol* **40**, 1357-69.

Futcher, A. B. and Cox, B. S. (1984). Copy number and the stability of 2-micron circle-based artificial plasmids of Saccharomyces cerevisiae. *J Bacteriol* **157**, 283-90.

Heiligenstein, X., Heiligenstein, J., Delevoye, C., Hurbain, I., Bardin, S., Paul-Gilloteaux, P., Sengmanivong, L., Regnier, G., Salamero, J., Antony, C. et al. (2014). The CryoCapsule: simplifying correlative light to electron microscopy. *Traffic* **15**, 700-16.

Henderson, B. R. (2005). Regulation of BRCA1, BRCA2 and BARD1 intracellular trafficking. *Bioessays* **27**, 884-93.

Huh, W. K., Falvo, J. V., Gerke, L. C., Carroll, A. S., Howson, R. W., Weissman, J. S. and O'Shea, E. K. (2003). Global analysis of protein localization in budding yeast. *Nature* **425**, 686-91.

Humphrey, J. S., Salim, A., Erdos, M. R., Collins, F. S., Brody, L. C. and Klausner, R. D. (1997). Human BRCA1 inhibits growth in yeast: potential use in diagnostic testing. *Proc Natl Acad Sci U S A* **94**, 5820-5.

Janke, C., Magiera, M. M., Rathfelder, N., Taxis, C., Reber, S., Maekawa, H., Moreno-Borchart, A., Doenges, G., Schwob, E., Schiebel, E. et al. (2004). A versatile toolbox for PCR-based tagging of yeast genes: new fluorescent proteins, more markers and promoter substitution cassettes. *Yeast* **21**, 947-62.

Jarosz, D. F. and Lindquist, S. (2010). Hsp90 and environmental stress transform the adaptive value of natural genetic variation. *Science* **330**, 1820-4.

Kaganovich, D., Kopito, R. and Frydman, J. (2008). Misfolded proteins partition between two distinct quality control compartments. *Nature* **454**, 1088-95.

Koszul, R., Kameoka, S. and Weiner, B. M. (2009). Real-time imaging of meiotic chromosomes in Saccharomyces cerevisiae. *Methods Mol Biol* **558**, 81-9.

Kraft, C., Kijanska, M., Kalie, E., Siergiejuk, E., Lee, S. S., Semplicio, G., Stoffel, I., Brezovich, A., Verma, M., Hansmann, I. et al. (2012). Binding of the Atg1/ULK1 kinase to the ubiquitin-like protein Atg8 regulates autophagy. *EMBO J* **31**, 3691-703.

Le Tallec, B., Barrault, M. B., Courbeyrette, R., Guerois, R., Marsolier-Kergoat, M. C. and Peyroche, A. (2007). 20S proteasome assembly is orchestrated by two distinct pairs of chaperones in yeast and in mammals. *Mol Cell* **27**, 660-74.

Lee, M. S., Green, R., Marsillac, S. M., Coquelle, N., Williams, R. S., Yeung, T., Foo, D., Hau, D. D., Hui, B., Monteiro, A. N. et al. (2010). Comprehensive analysis of missense variations in the BRCT domain of BRCA1 by structural and functional assays. *Cancer Res* **70**, 4880-90.

Mark, W. Y., Liao, J. C., Lu, Y., Ayed, A., Laister, R., Szymczyna, B., Chakrabartty, A. and Arrowsmith, C. H. (2005). Characterization of segments from the central region of BRCA1: an intrinsically disordered scaffold for multiple protein-protein and protein-DNA interactions? *J Mol Biol* **345**, 275-87.

Millot, G. A., Berger, A., Lejour, V., Boule, J. B., Bobo, C., Cullin, C., Lopes, J., Stoppa-Lyonnet, D. and Nicolas, A. (2011). Assessment of human Nter and Cter BRCA1 mutations using growth and localization assays in yeast. *Hum Mutat* **32**, 1470-80.

Milner, R., Wombwell, H., Eckersley, S., Barnes, D., Warwicker, J., Van Dorp, E., Rowlinson, R., Dearden, S., Hughes, G., Harbron, C. et al. (2013). Validation of the BRCA1 antibody MS110 and the utility of BRCA1 as a patient selection biomarker in immunohistochemical analysis of breast and ovarian tumours. *Virchows Arch* **462**, 269-79.

Orthwein, A., Noordermeer, S. M., Wilson, M. D., Landry, S., Enchev, R. I., Sherker, A., Munro, M., Pinder, J., Salsman, J., Dellaire, G. et al. (2015). A mechanism for the suppression of homologous recombination in G1 cells. *Nature* **528**, 422-6.

Perez-Valles, A., Martorell-Cebollada, M., Nogueira-Vazquez, E., Garcia-Garcia, J. A. and Fuster-Diana, E. (2001). The usefulness of antibodies to the BRCA1 protein in detecting the mutated BRCA1 gene. An immunohistochemical study. *J Clin Pathol* **54**, 476-80.

Ramos, P. C., Hockendorff, J., Johnson, E. S., Varshavsky, A. and Dohmen, R. J. (1998). Ump1p is required for proper maturation of the 20S proteasome and becomes its substrate upon completion of the assembly. *Cell* **92**, 489-99.

Rodriguez, J. A., Au, W. W. and Henderson, B. R. (2004). Cytoplasmic mislocalization of BRCA1 caused by cancer-associated mutations in the BRCT domain. *Exp Cell Res* **293**, 14-21.

Rutherford, S. L. and Lindquist, S. (1998). Hsp90 as a capacitor for morphological evolution. *Nature* **396**, 336-42.

Shulga, N., Mosammaparast, N., Wozniak, R. and Goldfarb, D. S. (2000). Yeast nucleoporins involved in passive nuclear envelope permeability. *J Cell Biol* **149**, 1027-38.

Sidorova, J. M. and Breeden, L. L. (1997). Rad53-dependent phosphorylation of Swi6 and down-regulation of CLN1 and CLN2 transcription occur in response to DNA damage in Saccharomyces cerevisiae. *Genes Dev* **11**, 3032-45.

Sikorski, R. S. and Hieter, P. (1989). A system of shuttle vectors and yeast host strains designed for efficient manipulation of DNA in Saccharomyces cerevisiae. *Genetics* **122**, 19-27.

Thompson, M. E. (2010). BRCA1 16 years later: nuclear import and export processes. *FEBS J* **277**, 3072-8.

Thompson, M. E., Robinson-Benion, C. L. and Holt, J. T. (2005). An amino-terminal motif functions as a second nuclear export sequence in BRCA1. *J Biol Chem* **280**, 21854-7.

Thouvenot, P., Ben Yamin, B., Fourriere, L., Lescure, A., Boudier, T., Del Nery, E., Chauchereau, A., Goldgar, D. E., Houdayer, C., Stoppa-Lyonnet, D. et al. (2016). Functional Assessment of Genetic Variants with Outcomes Adapted to Clinical Decision-Making. *PLoS Genet* **12**, e1006096.

Tulchin, N., Ornstein, L., Dikman, S., Strauchen, J., Jaffer, S., Nagi, C., Bleiweiss, I., Kornreich, R., Edelmann, L., Brown, K. et al. (2013). Localization of BRCA1 protein in breast cancer tissue and cell lines with mutations. *Cancer Cell Int* **13**, 70.

Tyedmers, J., Mogk, A. and Bukau, B. (2010). Cellular strategies for controlling protein aggregation. *Nat Rev Mol Cell Biol* **11**, 777-88.

Williams, R. S., Chasman, D. I., Hau, D. D., Hui, B., Lau, A. Y. and Glover, J. N. (2003). Detection of protein folding defects caused by BRCA1-BRCT truncation and missense mutations. *J Biol Chem* **278**, 53007-16.

Williams, R. S., Green, R. and Glover, J. N. (2001). Crystal structure of the BRCT repeat region from the breast cancer-associated protein BRCA1. *Nat Struct Biol* **8**, 838-42.

Wilson, C. A., Ramos, L., Villasenor, M. R., Anders, K. H., Press, M. F., Clarke, K., Karlan, B., Chen, J. J., Scully, R., Livingston, D. et al. (1999). Localization of human BRCA1 and its loss in high-grade, non-inherited breast carcinomas. *Nat Genet* **21**, 236-40.

Winzeler, E. A., Shoemaker, D. D., Astromoff, A., Liang, H., Anderson, K., Andre, B., Bangham, R., Benito, R., Boeke, J. D., Bussey, H. et al. (1999). Functional characterization of the S. cerevisiae genome by gene deletion and parallel analysis. *Science* **285**, 901-6.

Yu, X., Vazquez, A., Levine, A. J. and Carpizo, D. R. (2012). Allele-specific p53 mutant reactivation. *Cancer Cell* **21**, 614-25.

Zhao, X., Muller, E. G. and Rothstein, R. (1998). A suppressor of two essential checkpoint genes identifies a novel protein that negatively affects dNTP pools. *Mol Cell* **2**, 329-40.

Zimmermann, M., Lottersberger, F., Buonomo, S. B., Sfeir, A. and de Lange, T. (2013). 53BP1 regulates DSB repair using Rif1 to control 5' end resection. *Science* **339**, 700-4.

Figures

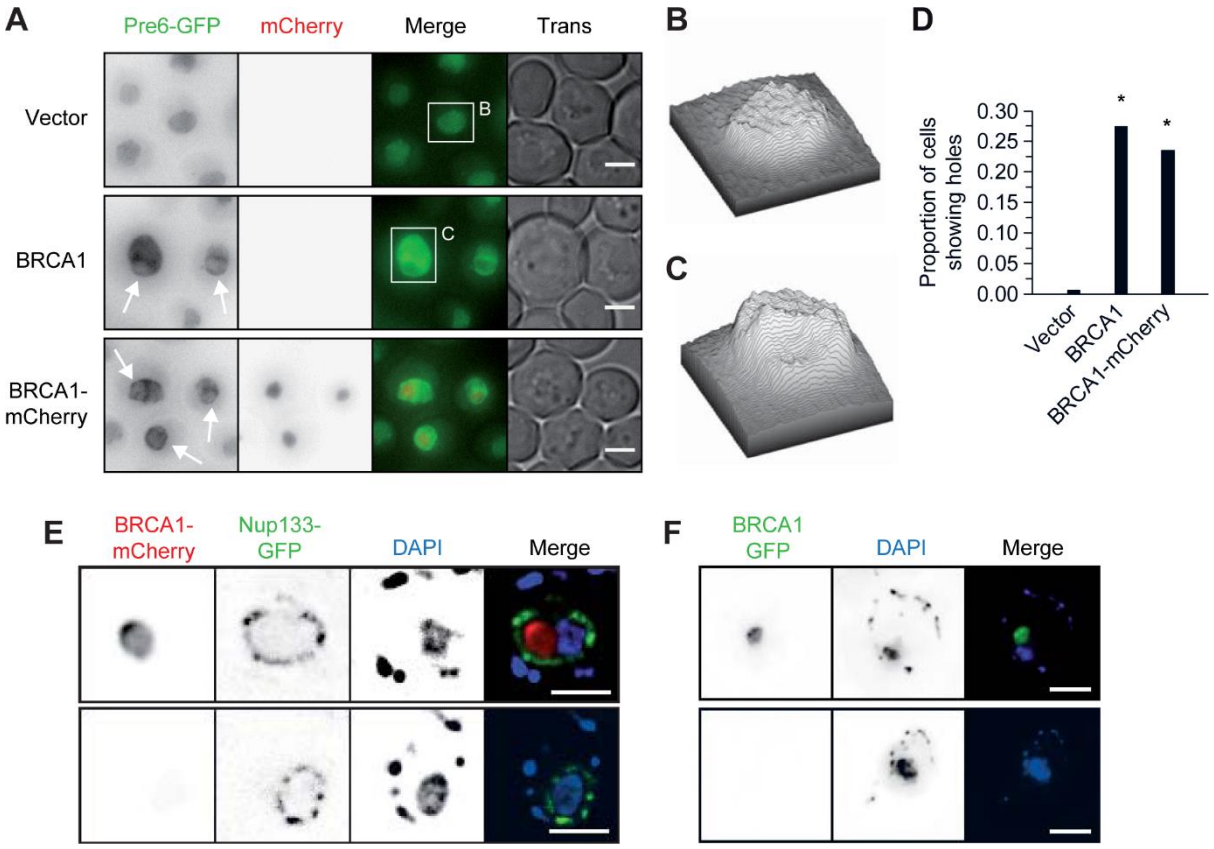

Fig. 1. The BRCA1 aggregates exclude large nuclear structures. (**A**) Accumulation of the proteasomal protein Pre6-GFP around BRCA1 aggregates. The depicted images result from live fluorescent microscopy analyses of Pre6-GFP cells expressing BRCA1 or BRCA1-mCherry. Pre6-GFP cells transformed with the vector plasmid are used as a negative control. Overlay images of GFP and mCherry signals (Merge) as well as transillumination images (Trans) are also shown. Arrows pinpoint the "hole" pattern observed. The number of cells analyzed is indicated in **Table S1**. Scale bars, 2 µm. (**B-C**) 3D representation of fluorescent intensities measured in the squares drawn in A. The "hole" pattern is present in the foreground of C. (**D**) Quantification of A (see **Table S1** for details, including sample sizes). The star indicates a significant difference in proportions compared to Vector cells (Fisher exact test). (**E-F**) Exclusion of the nuclear DNA from BRCA1 aggregates, using living Nup133-GFP cells expressing BRCA1-mCherry (**E**) or fixed wild type cells expressing BRCA1-GFP (**F**). Cells with (top) or without (bottom) nuclear aggregate come from the same picture acquisition. Pictures are representative of 96 (E, top panel) and 8 (F, top panel)

nuclear aggregates analyzed (100% exclusion). The nucleoporin Nup133-GFP allows the visualization of the nuclear membrane. DAPI stains the nuclear and mitochondrial DNA.

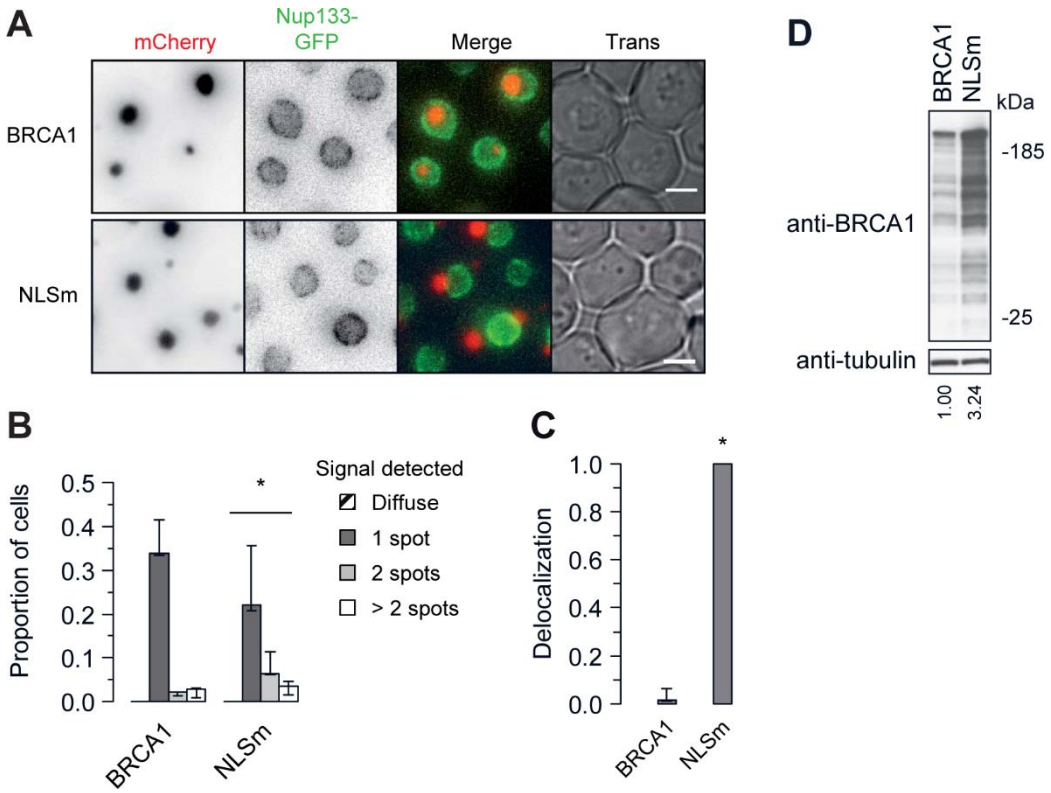

Fig. 2. NLSm-mCherry aggregates in the cytoplasm. (**A**) NLS inactivation of BRCA1-mCherry (NLSm) results in cytoplasmic localization of the protein. See **Fig. 1** for details. (**B**) Quantification of A (see **Table S1** for details, including sample sizes). The proportion of cells showing one fluorescent spot, two fluorescent spots, more than two fluorescent spots, or a diffusive signal, is depicted. Bars and whiskers correspond respectively to median and extreme values of three independent transformants. The star indicates a significant difference in median proportions compared to WT cells (Fisher exact test). (**C**) Proportion of fluorescent spots exclusively cytoplasmic (proportion of delocalization). Bars and whiskers correspond respectively to median and extreme values of the three independent transformants from B. The star indicates a significant shift of values compared to WT cells (MWW test). (**D**) The BRCA1 protein level is increased when aggregation occurs in the cytoplasm. Cell lysates were examined in Western blot for the presence of the BRCA1 protein (top panel). Tubulin was used as a loading control and was probed using an anti-Tubulin antibody on the same membrane after stripping the first labeling (bottom panel). Signal intensities of full lanes, relatively to the Tubulin band (normalized to 1 for BRCA1), are indicated below.

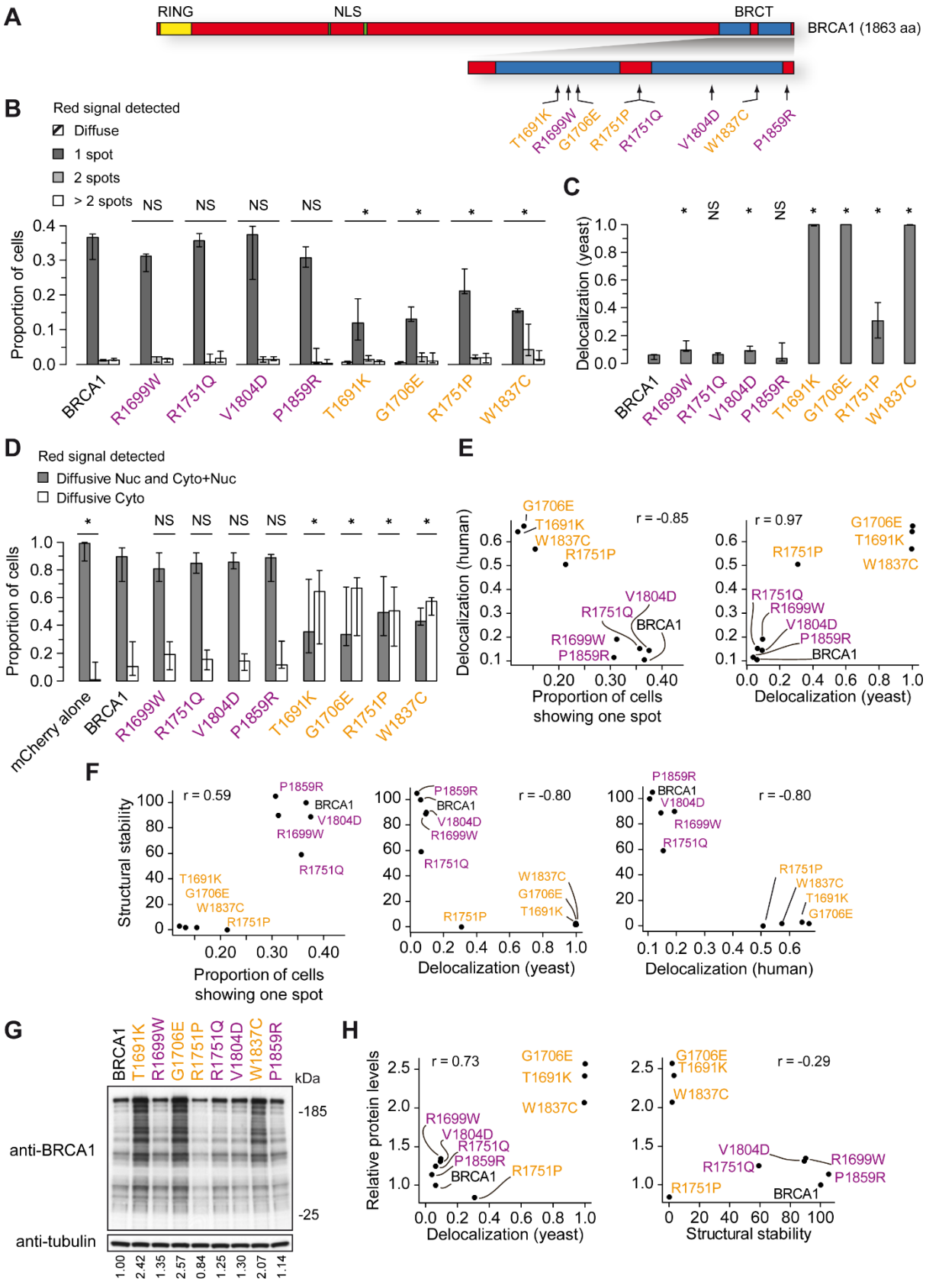

Fig. 3. Misfolding mutations impair the BRCA1 nuclear aggregation in yeast and the BRCA1 nuclear localization in human cells. (**A**) Schematic representation of the BRCA1 protein with positions of misfolding (orange) and non-misfolding (purple) missense mutations. (**B-C**) Misfolding mutations reduce the proportion of yeast cells showing one spot in fluorescent microscopy (**B**) and increase the cytoplasmic localization of the spots (**C**). See **Fig. 2B-C** and **Table S1** for details, including sample sizes. (**D**) Misfolding mutations decrease the proportion of RG37 human cells with BRCA1 nuclear localization. Following transient transfection and cell fixation, the ectopic expression of the WT or mutated mCherry-BRCA1 protein was visualized in fluorescent microscopy. Red cells were examined for the nuclear / nucleo-cytoplasmic localization, versus cytoplasmic localization of BRCA1. Bars and whiskers correspond respectively to median and extreme values of four independent transfections. The star indicates a significant difference in median proportions compared to WT cells (Fisher exact test, see **Table S1** for details). (**E**) Correlations between delocalization in human cells (white bars in D) and spot formation (dark bars in B), or between delocalization in human cells (white bars in D) and delocalization in yeast cells (bars in C). The Spearman coefficient of correlation is indicated. (**F**) Correlation between structural stability values and results described in E. The structural stability values were previously published (Lee et al., 2010) and correspond to the resistance of the BRCT domain to trypsin-mediated proteolysis *in vitro* (relatively to the WT BRCT set to value 100). (**G**) The BRCA1 protein level is increased when aggregation occurs in the cytoplasm of yeast cells. See **Fig. 2D** for details. (**H**) Correlation between relative protein levels (G) and delocalization in yeast cells (bars in C) or structural stability. The Spearman coefficient of correlation is indicated.

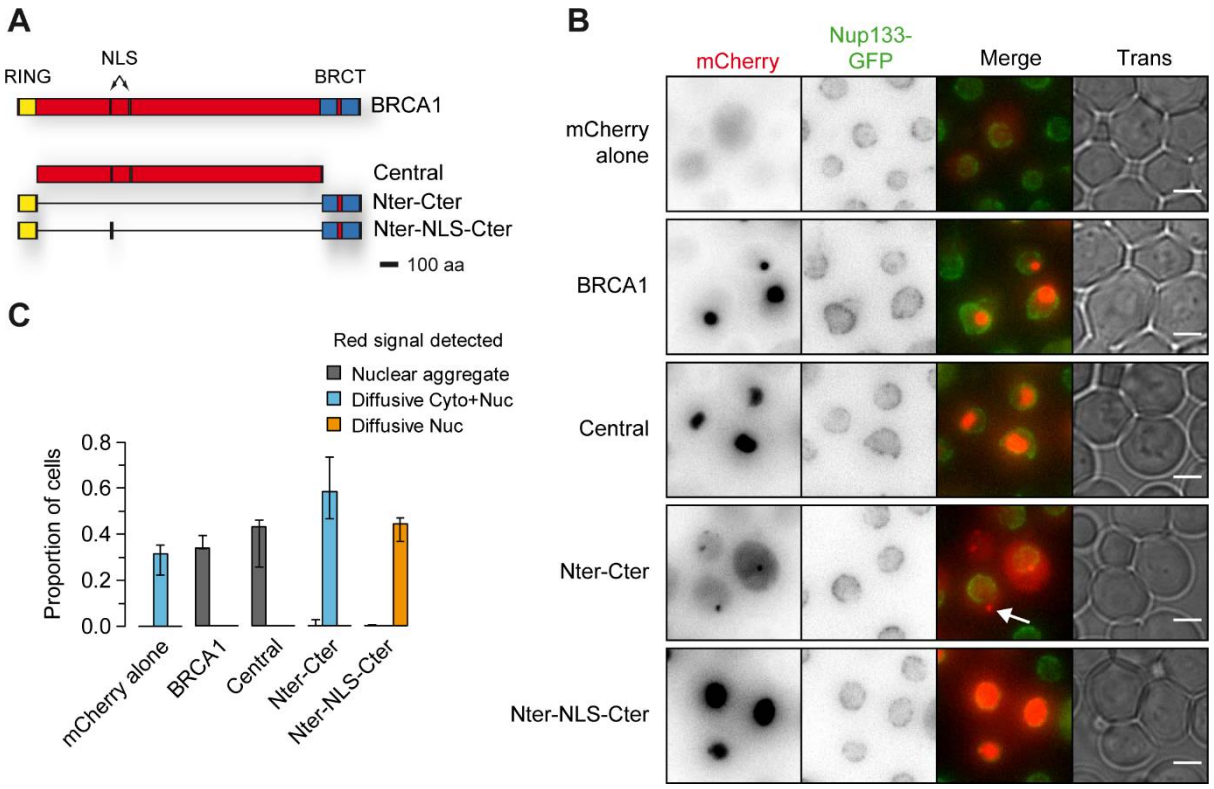

Fig. 4. The central part of BRCA1 alone is sufficient to promote nuclear aggregation in yeast. (**A**) Schematic representation of the BRCA1 protein and the generated truncations. Central, truncation of the amino acids 1 to 100 and 1652 to 1863, referred to as Δ(1-100; 1652-1863); Nter-Cter, Δ(101-1639); Nter-NLS-Cter: Δ(101-494; 517-1639). (**B**) The central part of BRCA1, but not the extremities, is required for the nuclear spot visualization in fluorescent microscopy. See **Fig. 1** for details. Cells expressing mCherry were used as a control for diffusive signals. (**C**) Quantification of B (see **Table S1** for details, including sample sizes). Bars and whiskers correspond respectively to median and extreme values of three independent transformants. The numbers of cells with 2 fluorescent spots and more than 2 fluorescent spots are not depicted but are as in **Fig. 3B** for the full length protein and null for the other constructs. 27% of the Nter-Cter-mCherry cells showing a diffusive signal in both the cytoplasm and nucleus presented an additional tiny fluorescent spot (white arrow). 17% of the Nter-NLS-Cter-mCherry cells showing a diffusive signal in the nucleus presented an additional tiny fluorescent spot in the cytoplasm. Cyto+Nuc, cytoplasm and nuclear localization; Nuc, nuclear localization.

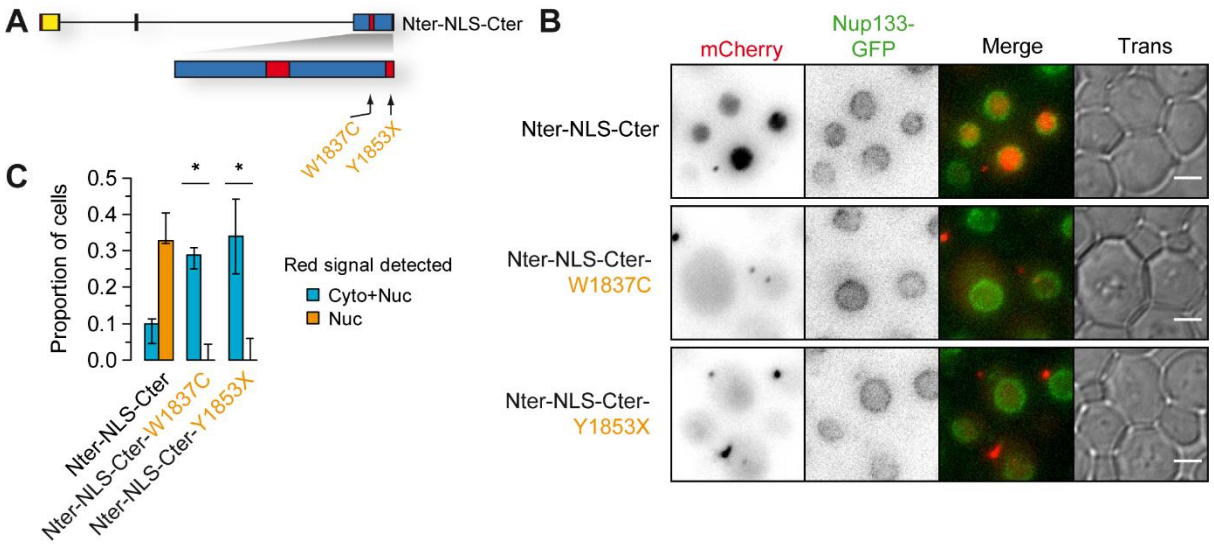

Fig. 5. Aggregation is not required for cytoplasmic relocalization induced by misfolding mutations. (**A**) Schematic representation of the Nter-NLS-Cter construction (see **Fig. 4A**) with positions of the misfolding mutations. (**B**) Images from fluorescent microscopy acquisitions showing the delocalization induced by misfolding mutations. See **Fig. 1** for details. (**C**) Quantification of B (see **Table S1** for details, including sample sizes). Bars and whiskers correspond respectively to median and extreme values of three independent transformants. The star indicates a significant difference in median proportions compared to WT cells (Fisher exact test). 23% of the Nter-NLS-Cter-mCherry cells showing a diffusive signal in the nucleus presented an additional tiny fluorescent spot in the cytoplasm. With W1837C and Y1853X, tiny fluorescent spots were visualized in respectively 44% and 35% of the cells showing a diffusive signal in both the cytoplasm and nucleus. The slight differences with **Fig. 4C** result from a better sensitivity used during picture acquisitions because of the absence of intense fluorescent spots. Cyto+Nuc, cytoplasm and nuclear localization; Nuc, nuclear localization.

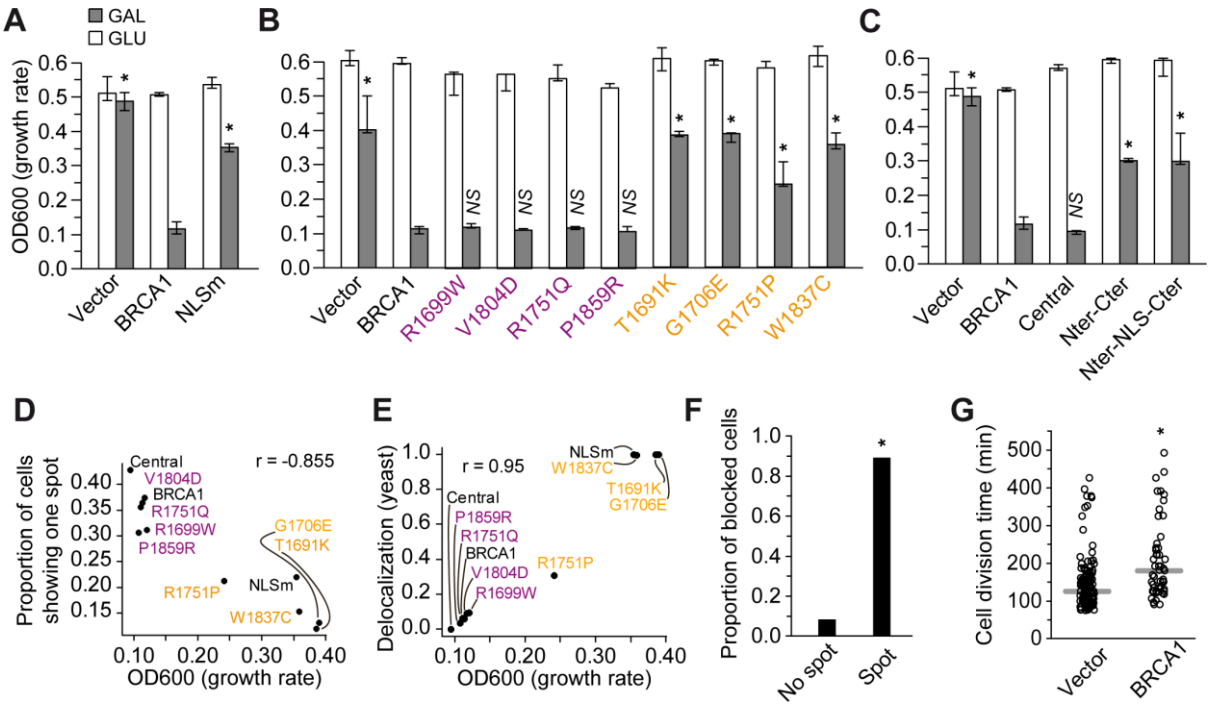

Fig. 6. Growth inhibition is associated with BRCA1 aggregation in the nucleus. (**A-C**) Growth inhibition is alleviated with NLS inactivation (**A**), misfolding missense mutations (**B**) or deletion of the central part of BRCA1 (**C**). See **Figs. 2-4** for details about the constructions. Liquid cultures of yeast cells started at identical cell concentration. Cells were grown in the presence of galactose (GAL) or glucose (GLU) for 15 hours and cell concentrations were measured by optical density at 600 nm, which reflects growth rate. One OD unit corresponds to 1.15×10^8 cells/ml. Galactose and glucose respectively induces and represses the expression of the WT or modified BRCA1 proteins. Vector cells were used as a control. Bars and whiskers correspond respectively to median and extreme values of three independent transformants. The star indicates a significant shift of values compared to WT cells (MWW test, see **Table S1** for details). (**D-E**) Correlation between cell growth and either proportion of cells showing one fluorescent spot (**D**) or proportion of cells with fluorescent spots exclusively cytoplasmic (**E**). The Spearman coefficient of correlation is indicated. These two plots compare the results from A-C (grey bars) and the results from **Figs. 2B-C**, **3B-C** and **4C**. (**F**) The nuclear aggregate is associated with a cell cycle arrest, as shown by single cell quantification of fluorescent videomicroscopy, using cells expressing WT BRCA1-mCherry (see **Movie S1**). No spot, no BRCA1 aggregate detected; Spot, BRCA1 aggregate detected; star, significant difference of the proportions (Chi-square test). (**G**) The cell division time is increased in cells expressing WT BRCA1, as shown by single cell quantification of transillumination videomicroscopy (see **Movies S2** and **S3**). Cells exhibiting

a cell-cycle arrest were excluded from this analysis. Grey horizontal bar: median. Star, significant shift of values (MWW test).

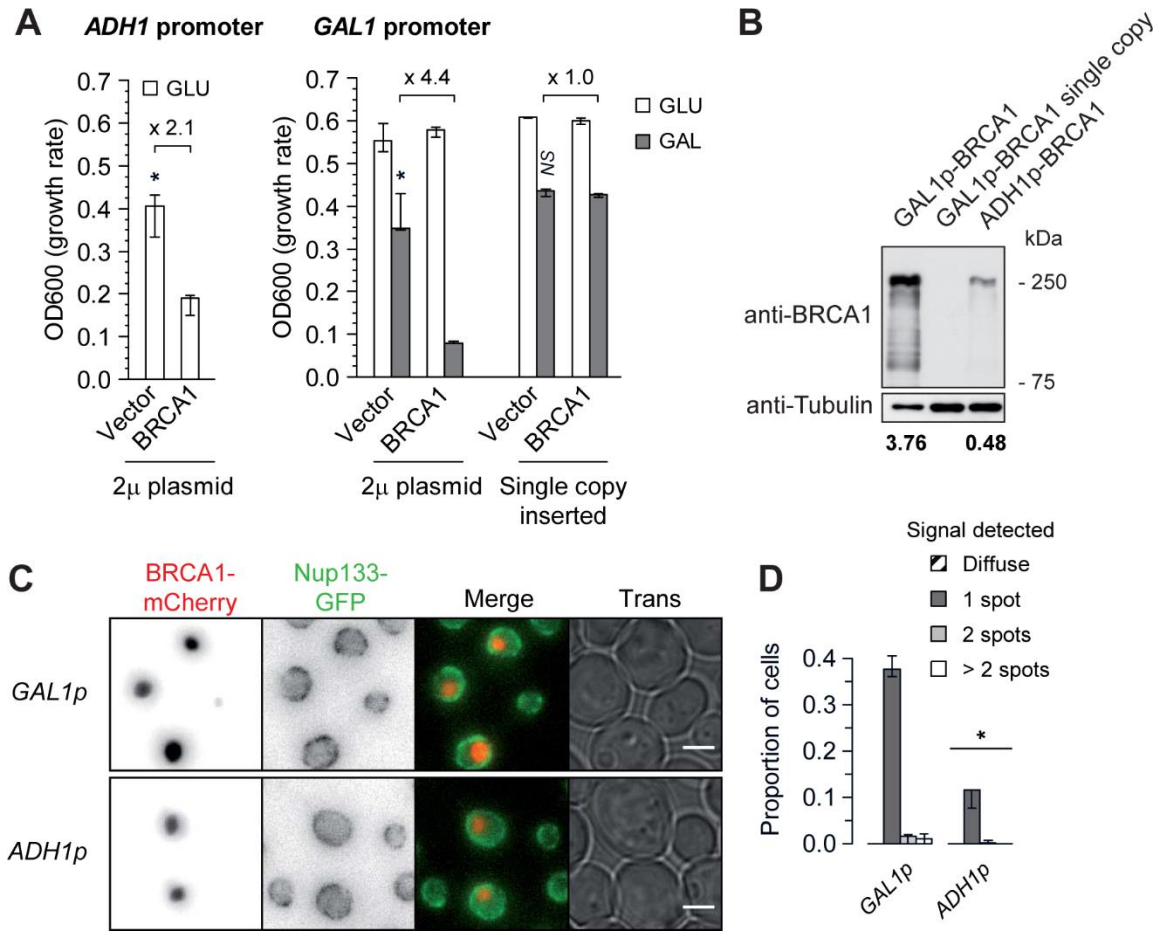

Fig. 7. A strong expression of BRCA1 is required for growth inhibition and formation of fluorescent spots. (**A**) The combination of the *GAL1* promoter (*GAL1p*) and 2µ plasmid induces a strong growth inhibition. Liquid cultures were performed as in **Fig. 6A-C**. Left panel, 2µ plasmid carrying the *BRCA1* cDNA under the control of the constitutive *ADH1* promoter (*ADH1p*). "Vector" refers to the same plasmid without cDNA inserted. Since the promoter is constitutively active, cells transformed with these plasmids were grown in the presence of glucose. Middle and right panels, *BRCA1* cDNA under the control of the *GAL1* promoter, inserted either in a 2µ plasmid (middle) or in the yeast genome (left). The star indicates a significant shift of values compared to BRCA1 cells (MWW test, see **Table S1** for details). (**B**) The combination of the *GAL1p* and 2µ plasmid induces strong BRCA1 protein levels. Cells from A were growth in glucose (*ADH1p*) or galactose (*GAL1p*) for 4 hours and cell lysates were examined as in **Fig. 2D**. (**C**) The combination of the *ADH1p* and 2µ plasmid reduces the formation of fluorescent spots. Nup133-GFP cells transformed with a 2µ plasmid carrying the *BRCA1-mCherry* cDNA under the control of the *GAL1* or *ADH1* promoter were grown for 4 hours with glucose (*ADH1p*) or galactose (*GAL1p*) before live fluorescent

microscopy analyses (see **Fig. 1** for details). (**D**) Quantification of C as in **Fig. 2B**. See **Table S1** for details, including sample sizes.

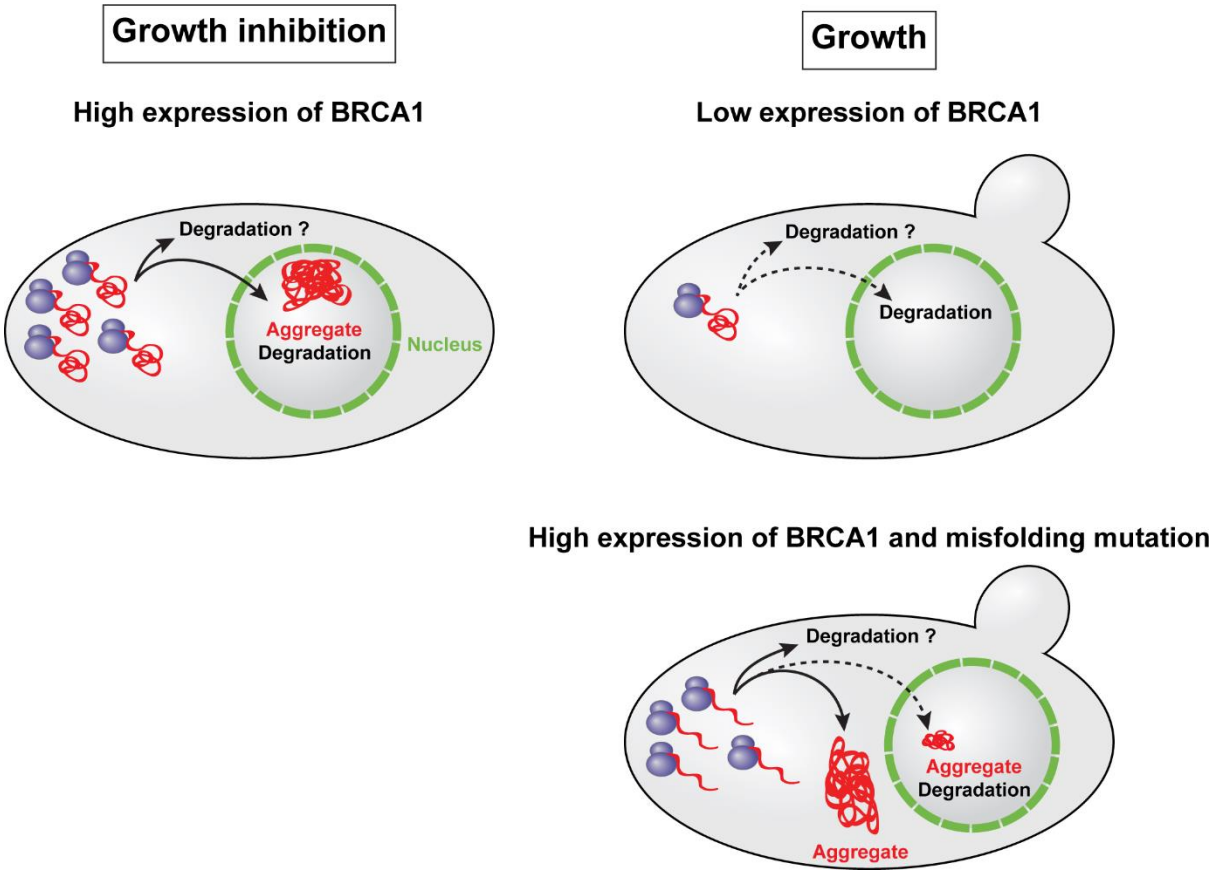

Fig. 8. Model depicting the underlying biological mechanisms of aggregation and growth inhibition used in the BRCA1 functional assays. Purple, ribosome; red, BRCA1 protein; green, nuclear membrane. Nuclear proteasome contributes, at least in part, to the degradation of the BRCA1 protein. Alternative mechanisms of degradation of BRCA1 remain to be investigated.

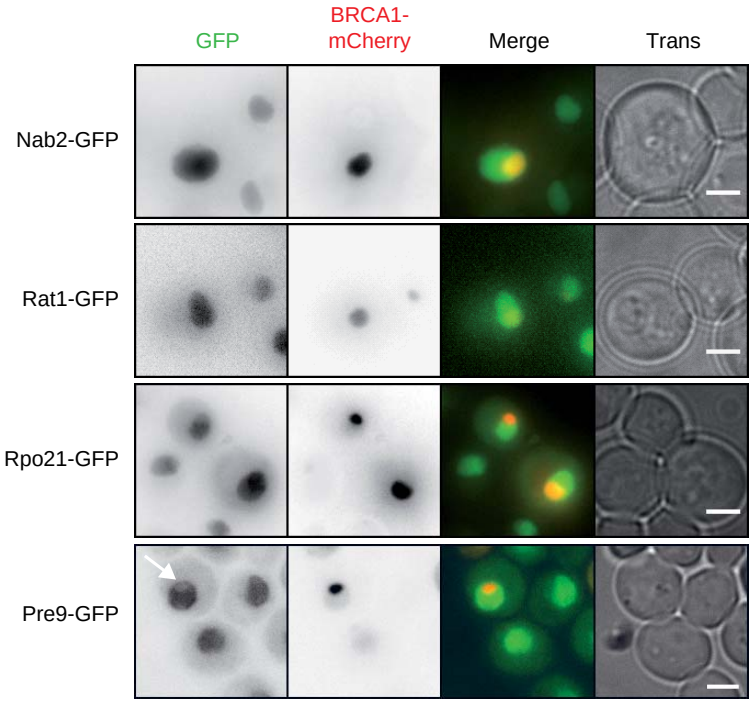

Fig. S1. The BRCA1 aggregate selectively excludes nuclear proteins. As in Fig. 1A. Nab2 is a nuclear polyadenylated RNA-binding protein, Rat1 is a nuclear 5' to 3' single-stranded RNA exonuclease, Rpo21 is the RNA polymerase II largest subunit and Pre9 is a component of the 20S core of the proteasome.

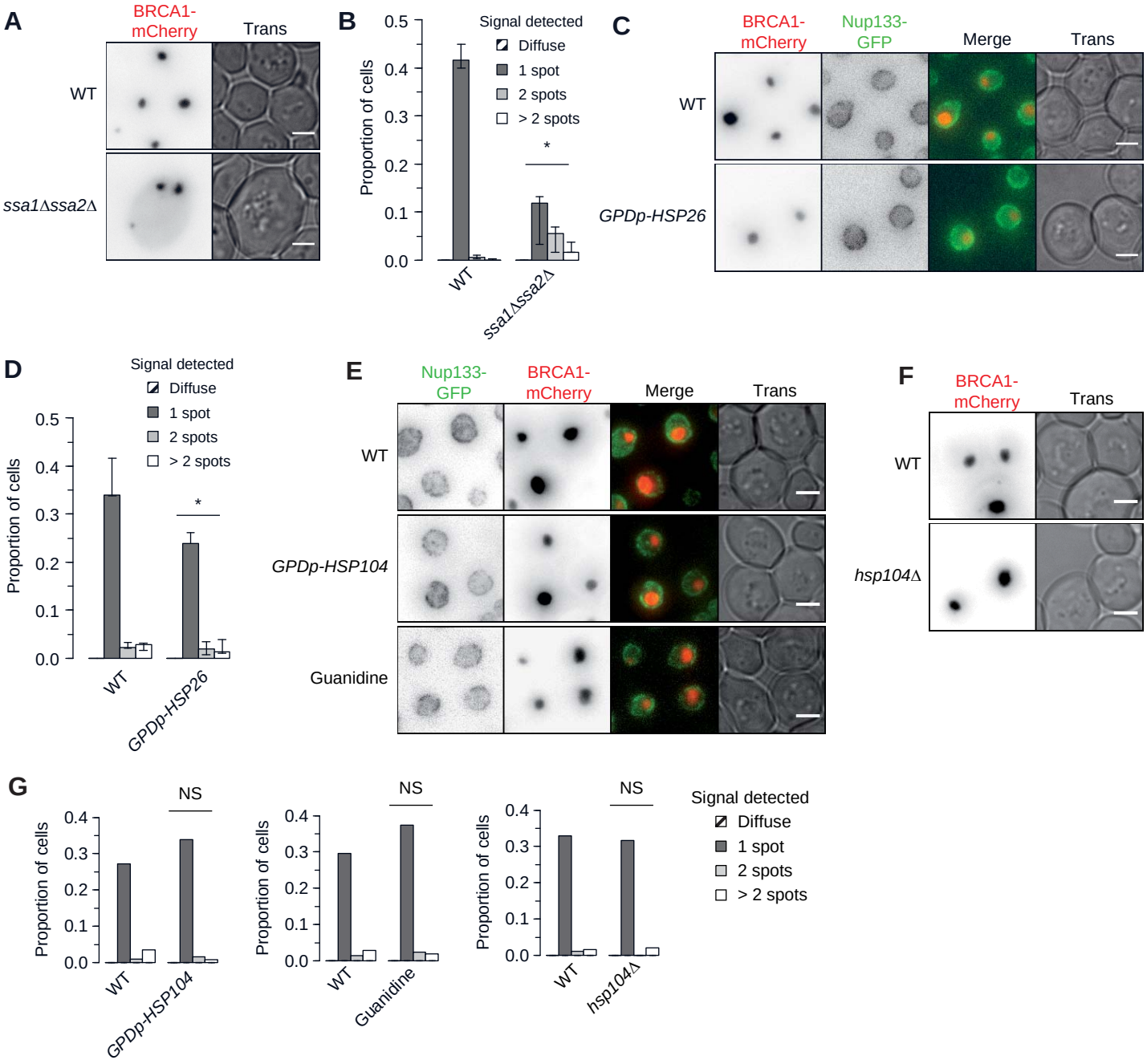

Fig. S2. The formation of the BRCA1-mCherry spot is influenced by chaperone proteins. See Fig. 1 for details. (**A**) The BRCA1-mCherry spot formation is impaired in cells deprived of Ssa1 and Ssa2 chaperones. These two chaperones are paralogs with a peptide sequence 98% identical. (**B**) Quantification of A (see Table S1 for details, including sample sizes). The proportion of cells showing one fluorescent spot, two fluorescent spots, more than two fluorescent spots, or a diffusive signal, is depicted. Bars and whiskers correspond respectively to median and extreme values of three independent transformants. The star indicates a significant difference in median proportions compared to WT cells (Fisher exact test). (**C**) The BRCA1-mCherry spot formation is decreased in cells overexpressing the Hsp26 chaperone. In these cells, the endogenous promoter of HSP26 has been replaced by the strong constitutive *GPD* promoter (*GPDp*). (**D**) Quantification of C as in B. (**E-F**) The Hsp104 chaperone has no clear influence on the BRCA1-mCherry spot formation. Overexpression of HSP104 (E), inhibition of Hsp104 by guanidine (E) and deletion of HSP104 (F) were examined. (**G**) Quantification of E-F as in B, except that a single transformant was analyzed. NS: no significant difference in proportions compared to WT cells (Fisher exact test).

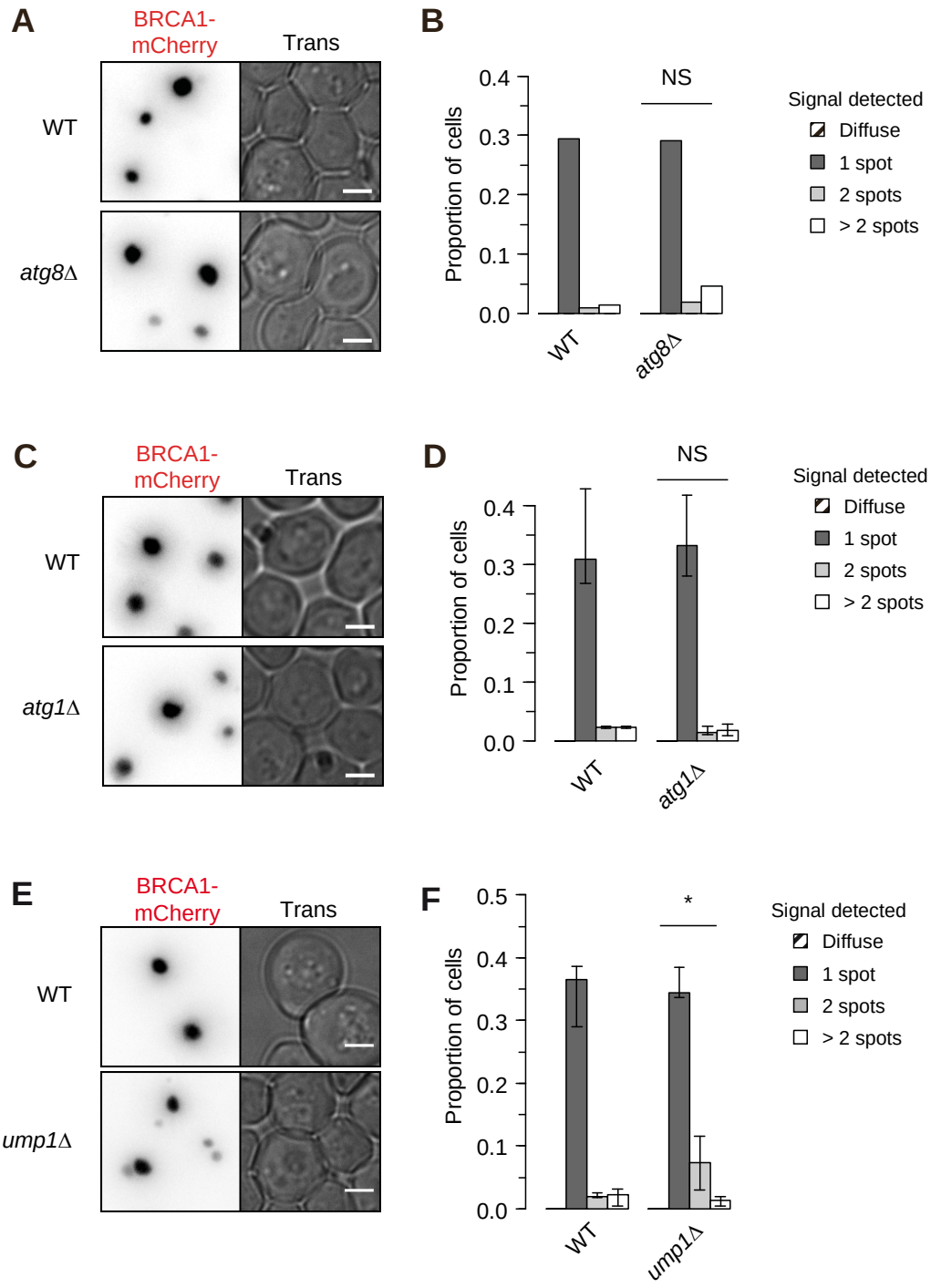

Fig. S3. The formation of the BRCA1-mCherry spot is influenced by proteolytic degradation. See Fig. S2 for details. (**A,C**) Autophagy has no clear influence on the BRCA1-mCherry spot formation, as shown by the deletion of *ATG8* (**A**) or *ATG1* (**C**) that impair the autophagy pathway. (**B**) Quantification of A (see Table S1 for details, including sample sizes). A single transformant was analyzed. (**D**) Quantification of C. Three independent transformants were analyzed. (**E**) Proteasome inactivation increases the BRCA1-mCherry spot formation, as shown by the deletion of *UMP1* that results in functionally impaired proteasomes. (**F**) Quantification of E. Three independent transformants were analyzed.

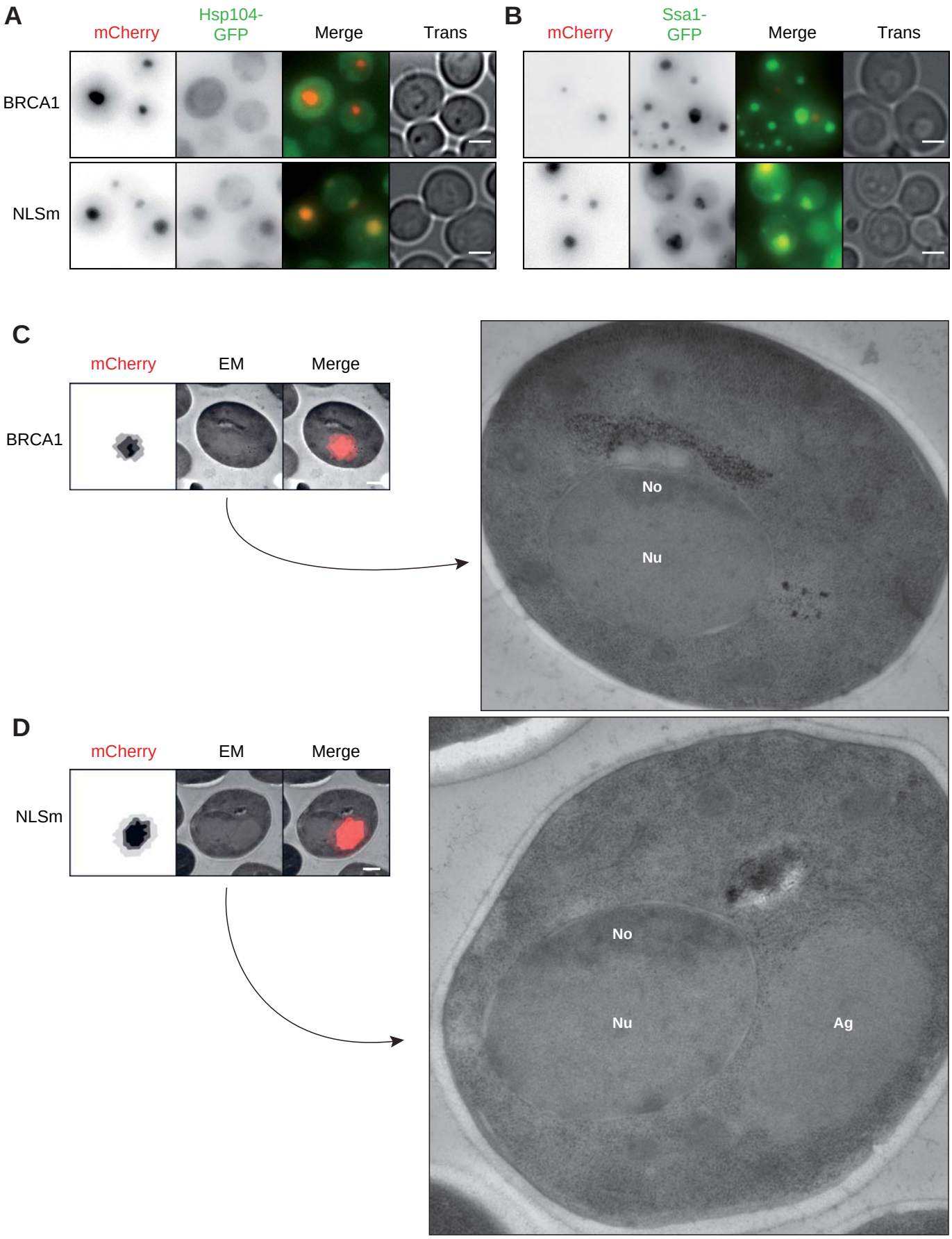

Fig. S4. The cytoplasmic BRCA1-mCherry aggregate is distinct from the nuclear aggregate. (**A**) Hsp104-GFP colocalizes with the cytoplasmic NLSm-mCherry aggregate, but not with the BRCA1-mCherry aggregate. (**B**) Ssa1-GFP accumulates around the cytoplasmic NLSm-mCherry aggregates, but not around the BRCA1-mCherry aggregate. (**C-D**) Cytoplasmic but not nuclear aggregates are visible in correlative light-electron microscopy (CLEM). Overlay images of fluorescent (mCherry) and electron microscopy (EM) are shown for cells expressing BRCA1-mCherry (**C**) or NLSm-mCherry (**D**). Scale bars, 1 µm. Nu, nucleus; No, nucleolus; Ag, aggregate.

Journal of Cell Science • Supplementary information

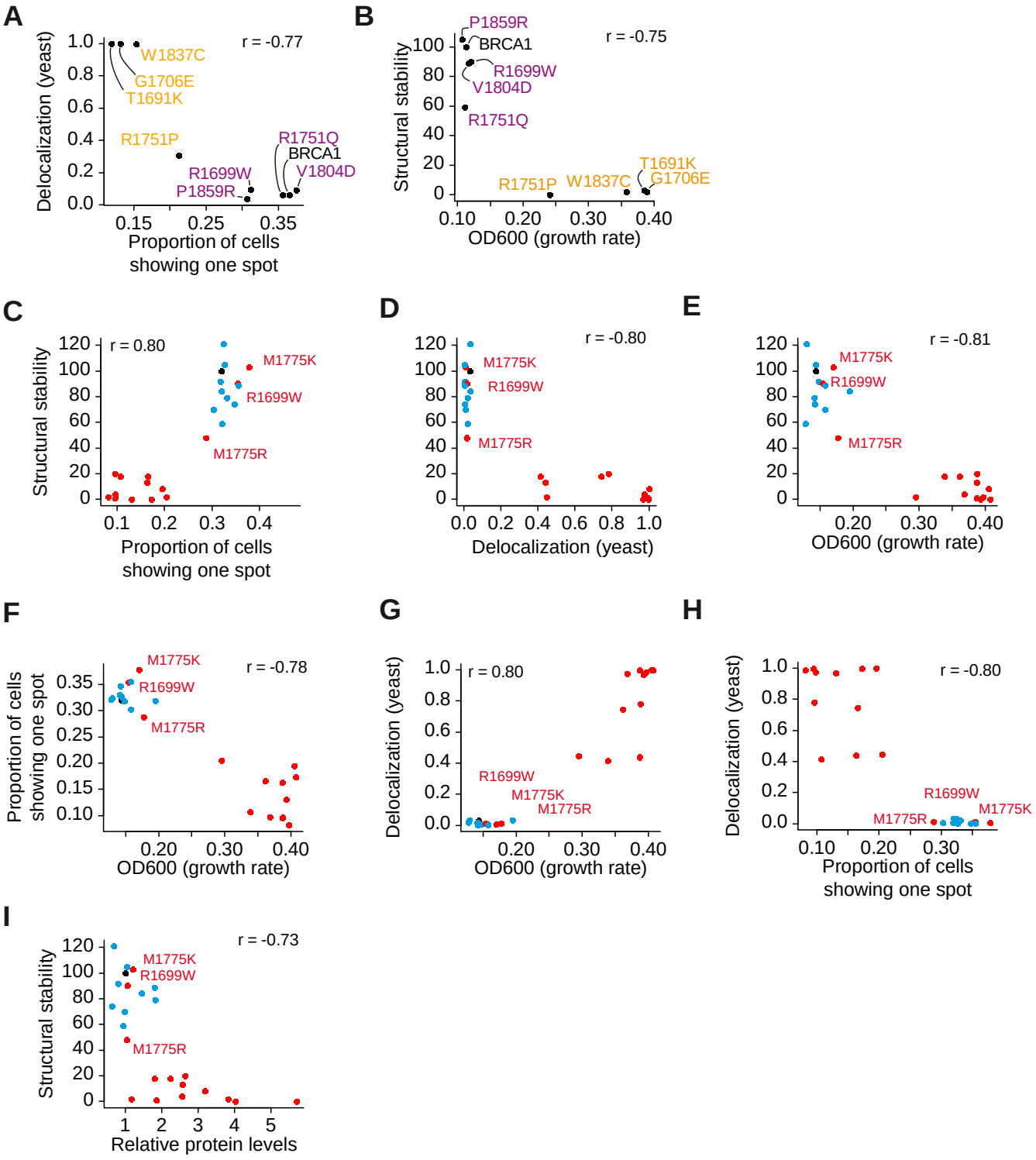

Fig. S5. Formation of fluorescent spots, spot delocalization and growth inhibition discriminate between misfolding and non-misfolding mutations of BRCA1. Spearman coefficients of correlation are indicated. (**A-B**) Supplementary correlations from Fig. 3 and Fig. 6. (**C-E**) Correlation between structural stability values (Lee et al., 2010) and results previously published (Thouvenot et al., 2016), using the Spot Formation (**C**), Yeast Localization (**D**) and Liquid Medium (**E**) assays. The Spot Formation assay exhibits the proportion of cells showing a single fluorescent spot. The Yeast Localization assay indicates the proportion of fluorescent spots exclusively cytoplasmic (proportion of delocalization). The Liquid Medium assay monitors the cell growth in liquid medium culture, as explained in Fig. 6A-C. The panel of 23 mutations shown includes the G1706E (orange) and the four R1699W, R1751Q, V1804D and P1859R (purple) mutations present in A-B, as well as 18 additional missense mutations (see also Table S2). Mutations were categorized as neutral or pathogenic according to genetic/epidemiological data. All of the pathogenic missense mutations strongly destabilize the BRCT domain, except R1699W, M1775K and M1775R (Lee et al., 2010). Red: pathogenic mutations blue, neutral mutation; black, WT BRCA1. (**F-H**) Correlation between Spot Formation, Yeast Localization and growth rate for the data shown in C-E. (**I**) Correlation between structural stability values and relative BRCA1 protein levels (Thouvenot et al., 2016).

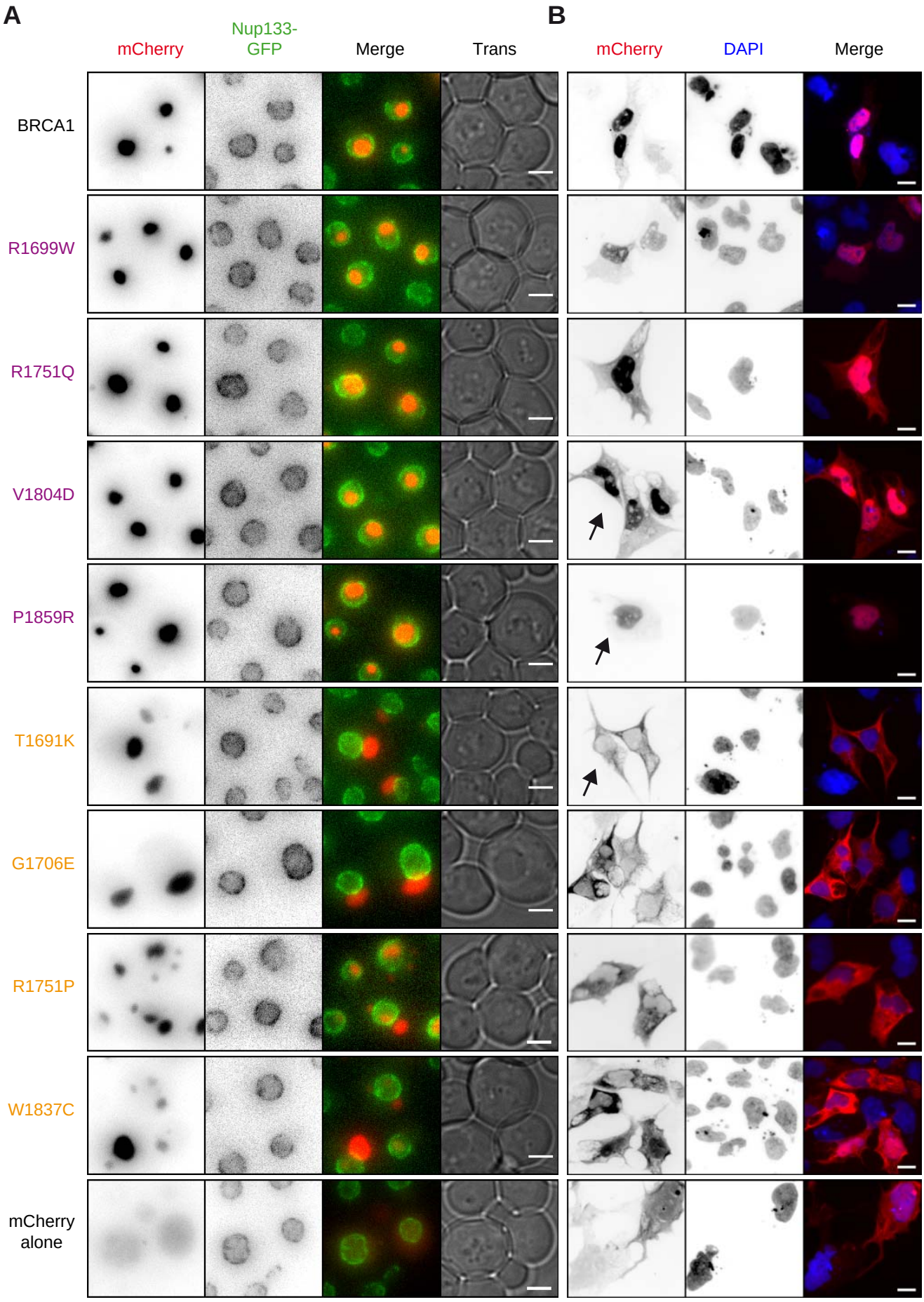

Fig. S6. Misfolding mutations are associated with BRCA1 cytoplasmic localization. Examples of fluorescent image acquisition in living yeast cells (**A**) or fixed human cells (**B**). In human cells, arrows show the distinction between nucleo-cytoplasmic, nuclear, and cytoplasmic localization of BRCA1 (in pictures 4 to 6 starting from the top, respectively).

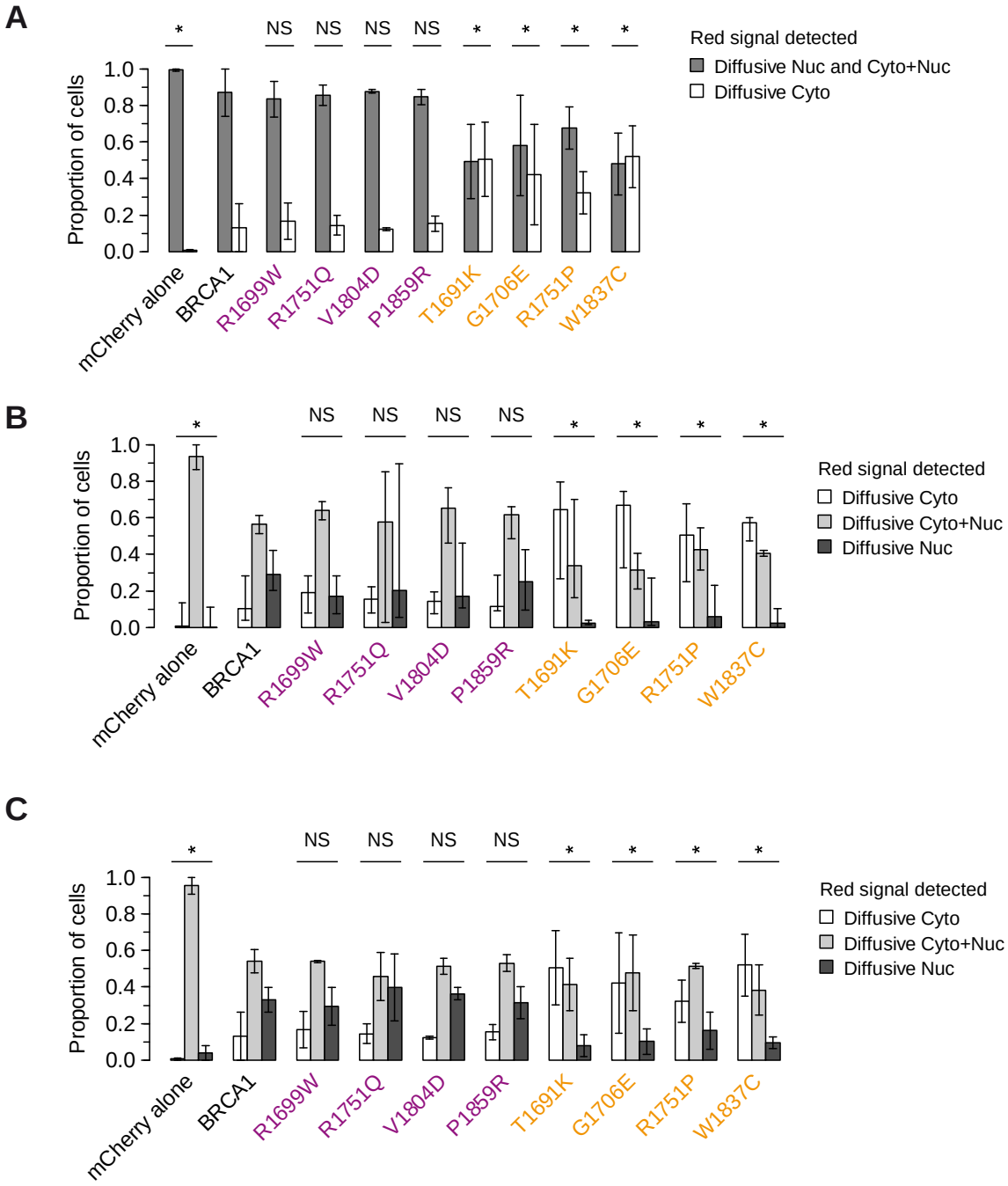

Fig. S7. Misfolding mutations of BRCA1 increase cytoplasmic localization in human cells. (**A**) As in Fig. 3D, except that RG37 cells were exposed to 10 Gy ionizing radiation, 24h after transfection, and were subsequently grown for 4/7 hours before labeling. Bars and whiskers correspond respectively to median and extreme values of two independent transfections. (**B**) Results from Fig. 3D separated in three classes. (**C**) Results from **A** separated in three classes.

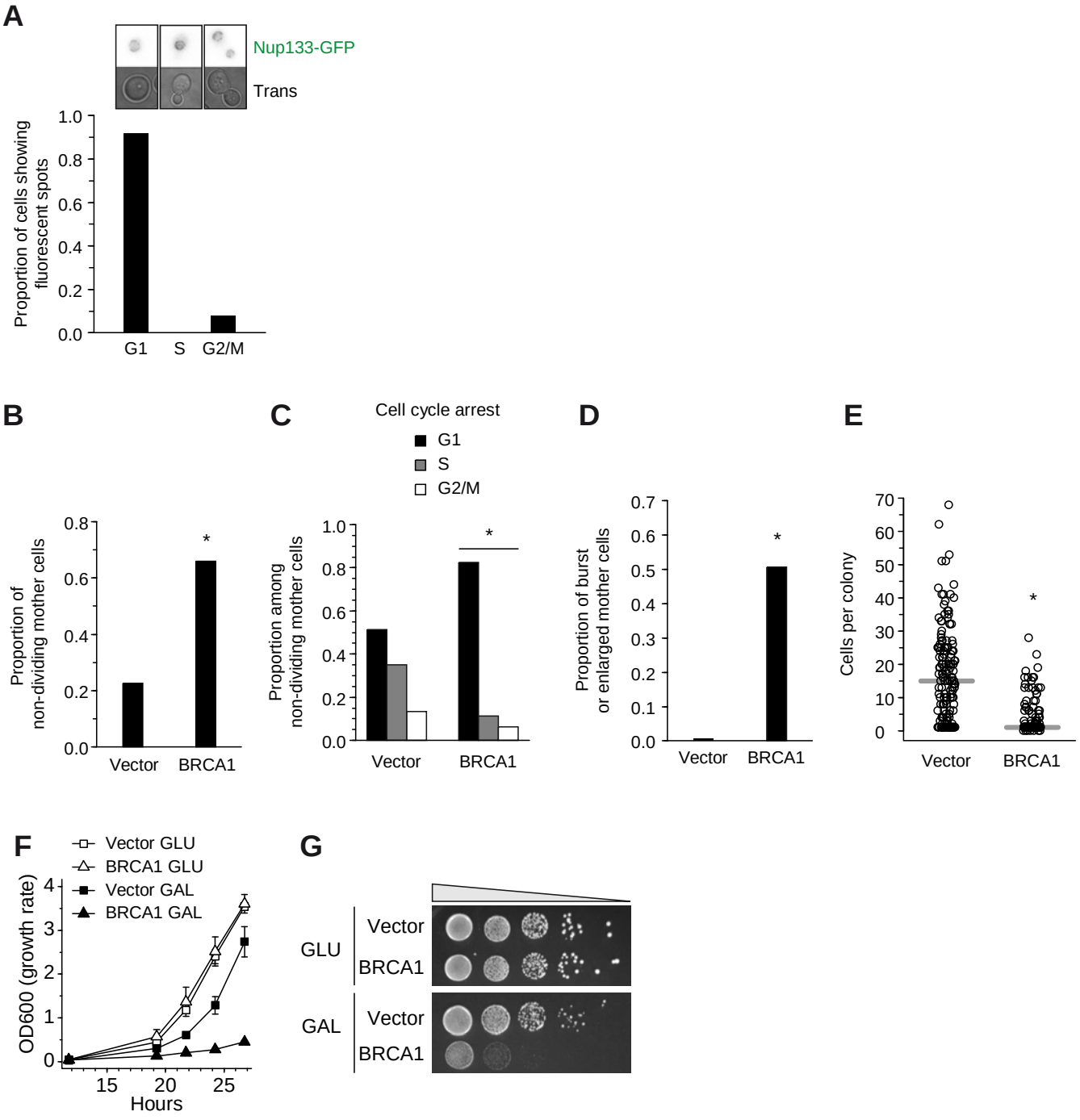

Fig. S8. Growth inhibition monitored in bulk cell is a combination of slow-dividing and non-dividing cells. (**A**) Fluorescent videomicroscopy of cells expressing WT BRCA1-mCherry (see Movie S1) showing that cells exhibiting the BRCA1 aggregate are blocked in G1. Top panel, cell morphology giving the phase: no bud (G1) or small bud with no nucleoporin Nup133-GFP (S) or a bud more than half the size of the mother cell + Nup133-GFP (G2/M). (**B-E**) Growth rate analysis of individual cells using transillumination videomicroscopy (see Movie S2). Graphs show the results of three independent transformants pooled. Star, significant differences (see Table S1 for details, including sample sizes). Vector cells were used as a control. In B, the high number of non-dividing cells for Vector cells probably reflects the stressful condition of videomicroscopy experiments. Increased size and cell burst in D suggests a severe metabolic disorder. Grey horizontal bar in E: median. (**F**) Long term liquid cultures of yeast cells started at identical cell concentrations. Cells expressing BRCA1 were grown in the presence of galactose (GAL) or glucose (GLU) for 27 hours and cell concentrations were measured by optical density at 600 nm (growth rate) at indicated times. Results represent the means ± standard deviations of three independent transformants. One OD corresponds to 1.5×10^7 cell /ml. (**G**) Drop test assay. Increasing concentrations of cells were plated on GLU- or GAL-containing medium and grown for 48 hours before picture acquisition.

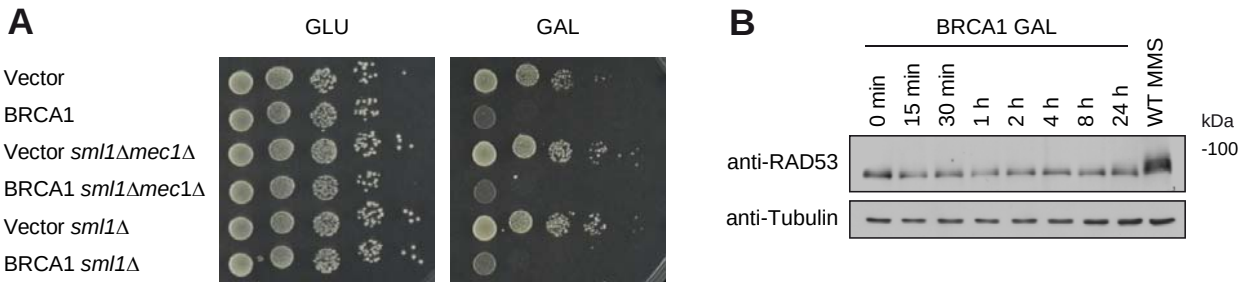

Fig. S9. Growth inhibition is not related to Mec1-dependent checkpoint activation. (**A**) Growth inhibition is not restored in *mec1*Δ cells expressing BRCA1. Drop test assay as in Fig. S8G. Deletion of *SML1* confers viability to *mec1*Δ cells (Zhao et al., 1998). (**B**) Rad53 is not phosphorylated in cells expressing BRCA1. Western blot analysis as in Fig. 2D. As a positive control, WT yeast cells were incubated with methyl methanesulfonate (MMS) 0.01% for 6 hours. Phosphorylation is visualized by a shifted band. Mec1-dependent phosphorylation of Rad53 is a critical step of checkpoint activation (Berens and Toczyski, 2012).

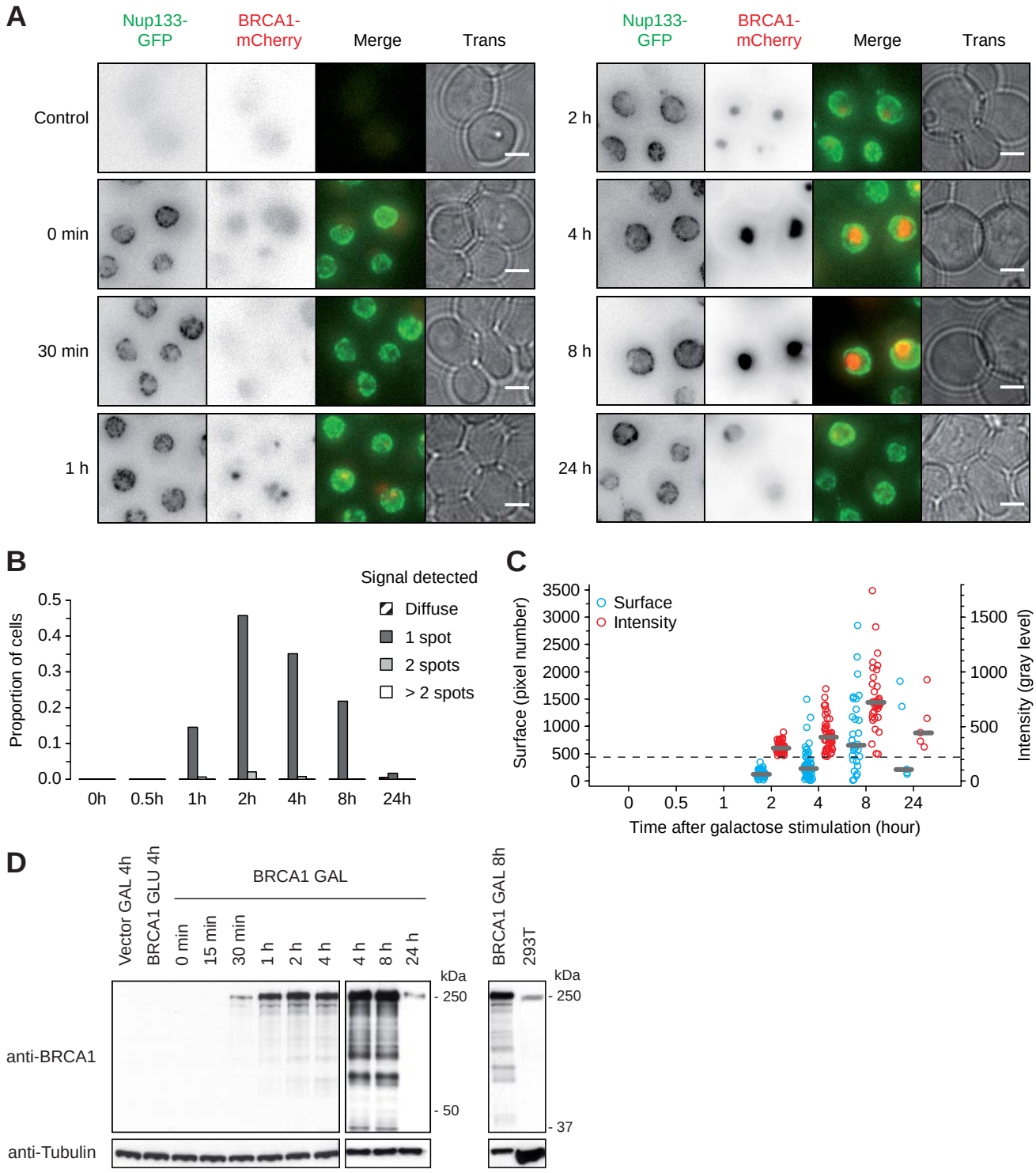

Fig. S10. The nuclear BRCA1-mCherry spot is transiently detected in time course experiments. (**A**) Example of picture acquisition. Nup133-GFP cells expressing BRCA1-mCherry were induced with galactose during the indicated time before live fluorescent microscopy analyses. Yeast cells expressing BRCA1 were used as a negative control of fluorescence. See Fig. 1 for details. Left panels, the range of pixel values in the red 12-bit images was set to 115-160, meaning that a pixel with a value equal or below 115 is white and a pixel with a value equal or over 160 is black. Right panels, range set to 115-400. (**B**) Proportion of cells that exhibit mCherry signals in fluorescence microscopy. A minimum of 150 cells were monitored per time point. (**C**) Spot quantification. Spots detected in the red fluorescent channel were delimited using the ImageJ software. Spot surface (pixel number, blue open circle and left y-axis) and maximum intensity (value of the pixel with the maximum intensity inside the delimited spot area, red open circle and right y-axis) of each spot was then quantified. Median values are indicated by horizontal grey segments. The dotted line pinpoints the threshold used to delimit the spots (minimum pixel value = 220). Decreasing this threshold increased the spot surface and below 220, spots started to overlap. Absence of dots for 1 hour of galactose stimulation indicates that all the spots visualized in B have pixel values below 220. Surface of one pixel: 4160 nm^2. (**D**) Western blot analysis (see Fig. 2D for details). Cells expressing BRCA1 were induced with galactose (GAL) or glucose (GLU) for the indicated time. Lysates from the human 293T cell line provided the expected size of the full-length BRCA1 protein.

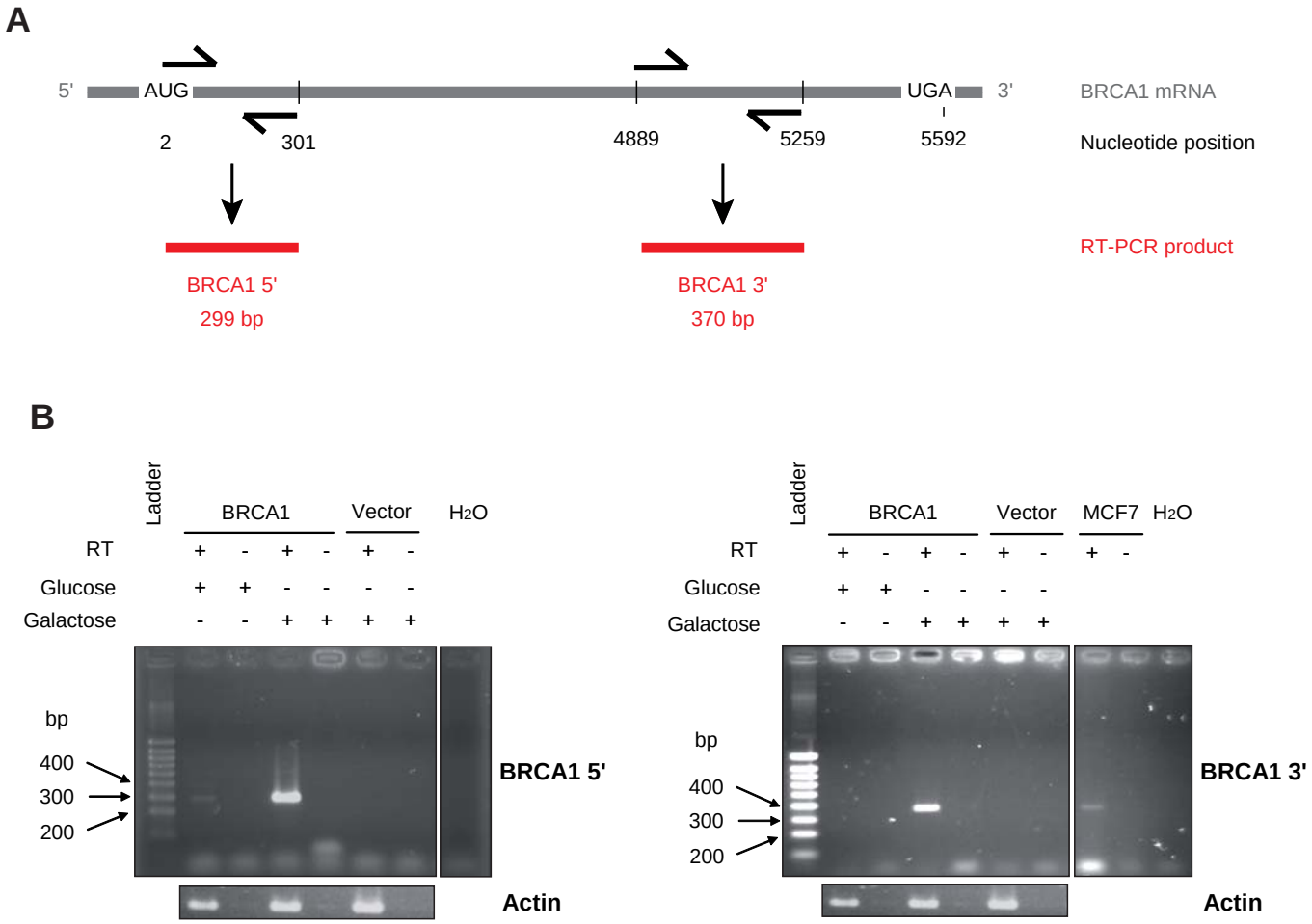

Fig. S11. The *BRCA1* mRNA is detected in yeast cells carrying the *GAL1p-BRCA1* construct integrated at a single copy in the genome. (**A**) Schematic of the primers used and RT-PCR products obtained. Left, BRCA1-5' primer couple amplifying a 299 base pair (bp) sequence located between nucleotide 2 and 301 in the 5592 nucleotide-long *BRCA1* mRNA coding sequence (starting at nucleotide A of the AUG and ending at nucleotide A of the UGA stop codon). Right, BRCA1-3' primer couple amplifying a 370 bp sequence located between nucleotide 4889 and 5259. (**B**) RT-PCR results. Cells were stimulated for 12 hours with glucose or galactose prior to RNA extraction and RT-PCR analysis on agarose gel. An equivalent of 6 ng of RNA were loaded per well. Left panel, BRCA1-5' primer couple. Right panel, BRCA1-3' primer couple. Actin, primer couple specific to *Actin* mRNA used as a control of RNA presence. RT, reverse transcriptase added (+) or not (-) during reverse transcription to detect any DNA contamination; MCF7, RNA from human MCF7 cells used as a positive control; H2O, negative PCR control.

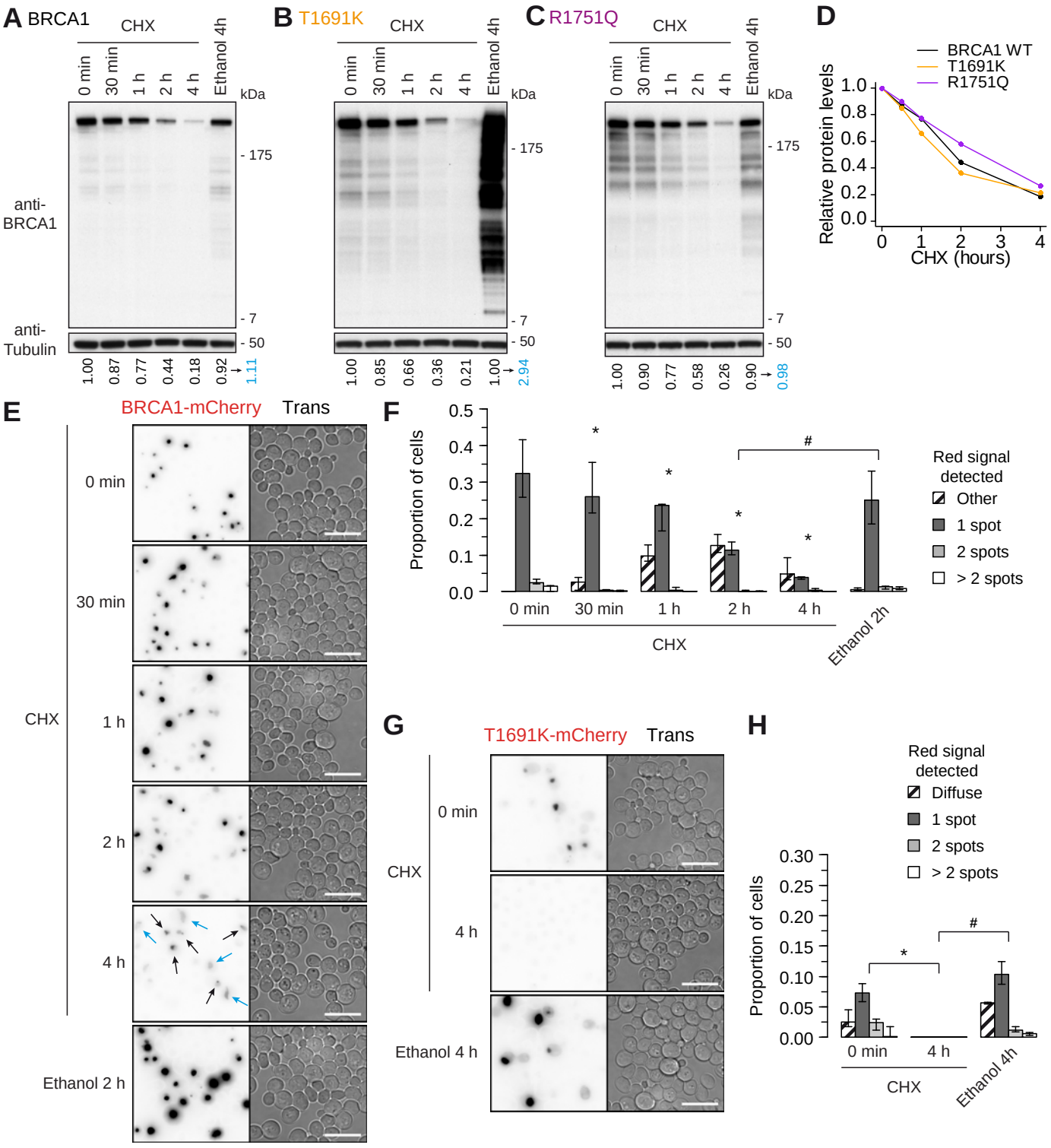

Fig. S12. The WT or mutated BRCA1 proteins are unstable in yeast cells. (**A-C**) Western blot analyses showing the instability of the WT or mutated BRCA1 proteins in *PDR5* deficient yeast cells. Deletion of the plasma membrane transporter gene *PDR5* increases the sensitivity of yeast cells to xenobiotics, such as the translational inhibitor cycloheximide (CHX). *PDR5* deficient cells transformed with a 2µ - *GAL1* promoter expression plasmid were induced for 2 hours with galactose to initiate the synthesis of the WT BRCA1-mCherry (**A**), T1691K-mCherry (**B**) or R1751Q-mCherry protein (**C**). Then, CHX diluted in pure ethanol was incorporated to the culture for the indicated time and cell lysates were examined as in Fig. 2D. Ethanol treatment is a control exhibiting the protein levels obtained after 4 hours of culture without CHX (six hours of galactose induction totally). Signal intensities of the top band, relatively to the Tubulin band (normalized to 1 for time 0 min), are indicated below. Signal intensities of the whole lane relatively to the Tubulin band (normalized to 1 for time 0 min) is indicated for the Ethanol control by a blue number, which provides a comparison of the whole BRCA1 peptide levels between two hours and six hours of galactose induction. (**D**) Plot of the black values shown in A-C. (**E**) Instability of the fluorescent spot in *PDR5* deficient cells expressing the WT BRCA1-mCherry protein. Cells were treated as described in A-D (except 2 hours instead of 4 hours for the "Ethanol" control) before analysis using live microscopy. Fluorescent mCherry signals as well as transillumination images (Trans) are shown. Scale bars, 10 µm. See Fig. S10A that depicts the increase of spot surface and spot intensity between two hours (here time 0 min, top panel) and four hours (here Ethanol 2 hours, bottom panel) of galactose induction. Arrows show examples of spot shape alterations after 4 hours of CHX treatment. Black arrow, single fluorescent spot embedded in a subcellular diffusive signal; blue arrow, faint / twisted spot. (**F**) Quantification of E (see Table S1 for details, including sample sizes). The "1 spot" category includes the single fluorescent spot embedded in a subcellular diffusive signal depicted in E. "Other" refers to peculiar signals, mostly the faint and twisted fluorescent spots shown in E. Star, significant differences in median proportions compared to time 0 min; hash, significant differences in median proportions between CHX 2 hours and Ethanol 2 hours (Fisher exact test). (**G-H**) Instability of the fluorescent spot in *PDR5* deficient cells expressing T1691K-mCherry. As in E and F, except that the Ethanol treatment lasted four hours and except the "Diffuse" category instead of the "Other" category.

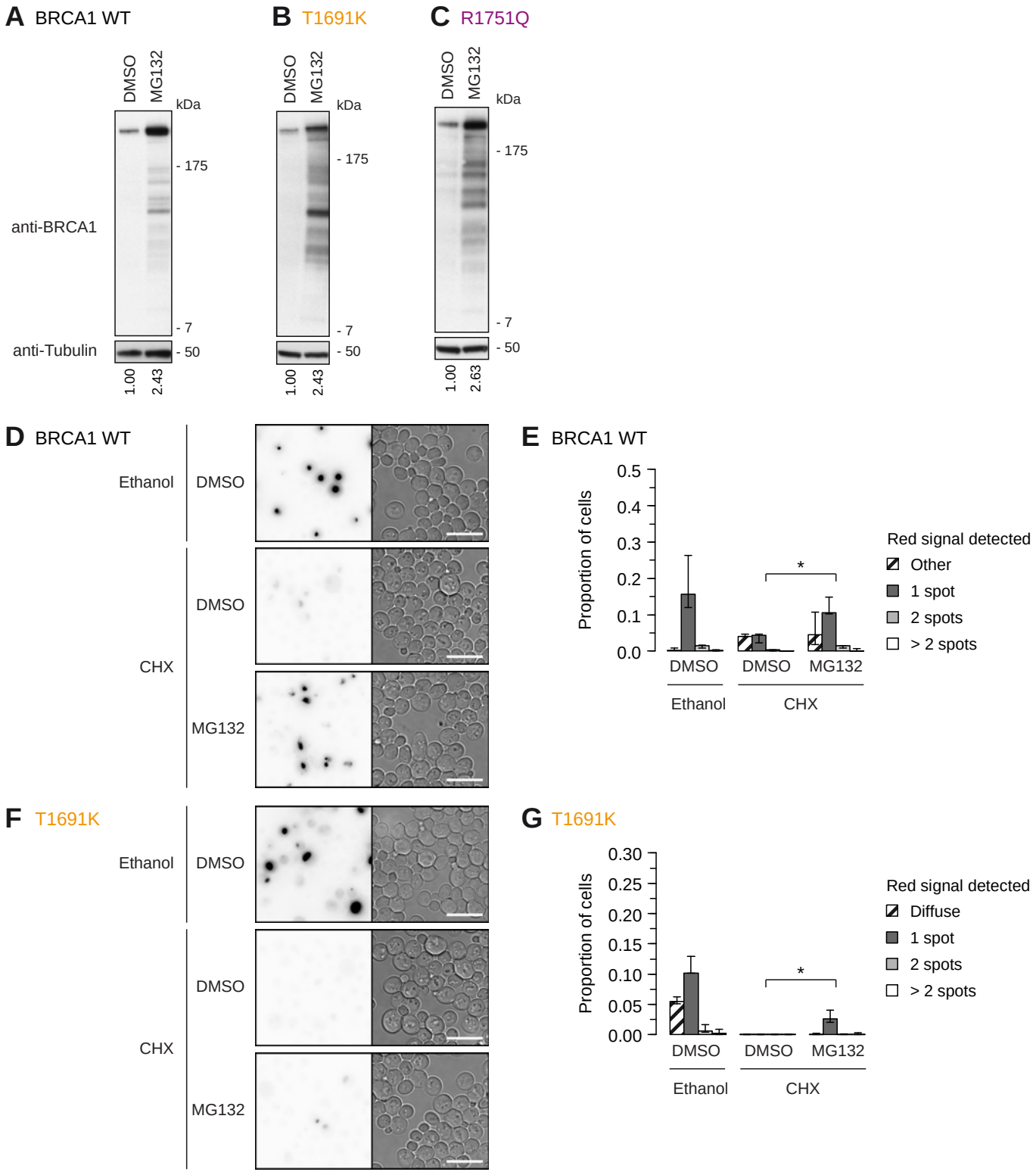

Fig. S13. Proteasome inhibition stabilizes the WT and mutated BRCA1 protein levels. (**A-C**) Western blot analyses showing the stabilization of the WT BRCA1-mCherry (**A**), T1691K-mCherry (**B**) or R1751Q-mCherry protein (**C**). *PDR5* deficient cells transformed with a 2µ - *GAL1* promoter expression plasmid were induced for 2 hours with galactose supplemented with proteasome inhibitor MG132 diluted in pure DMSO. Then, CHX diluted in pure ethanol was incorporated to the culture for four additional hours and cell lysates were examined as in Fig. 2D. DMSO instead of MG132 was used as a control of CHX treatment (equivalent to the "CHX 4 h" panel in Fig. S12A). Signal intensities of the top band, relatively to the Tubulin band (normalized to 1 for DMSO), are indicated below. (**D**) Stabilization of the fluorescent spot in *PDR5* deficient cells expressing the WT BRCA1-mCherry protein. Cells were treated as described in A-C before analysis using live microscopy. Fluorescent mCherry signals as well as transillumination images (Trans) are shown. Scale bars, 10 µm. DMSO instead of MG132 was used as a control of CHX treatment (middle panel, equivalent to the "CHX 4 h" panel in Fig. S12E). Ethanol instead of CHX was used as a control of fluorescent spot formation without treatments (top panel, six hours of galactose induction, totally). (**E**) Quantification of D using the categories described in Fig. S12F (see Table S1 for details, including sample sizes). Star, significant differences in median proportions between the MG132 and the DMSO control treatments (Fisher exact test). (**F-G**) Stabilization of the fluorescent spot in *PDR5* deficient cells expressing T1691K-mCherry. As in D and E, except the "Diffuse" category instead of the "Other" category.

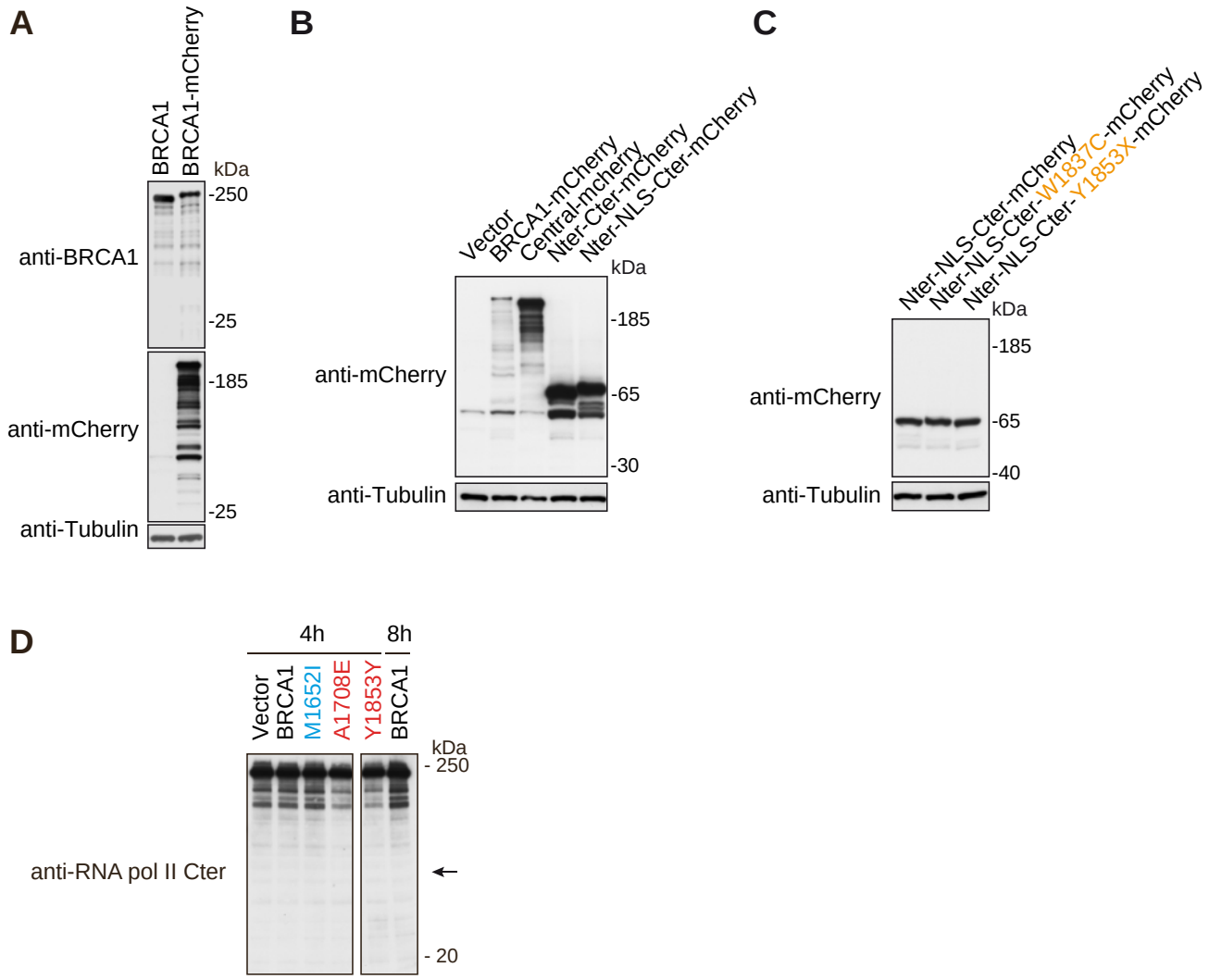

Fig. S14. Additional Western-blot analyses. (**A-C**) Protein levels for truncated forms of BRCA1. Cell lysates were examined by Western blot for the presence of the BRCA1 or the mCherry protein (indicated on the left side of panels). The anti-mCherry antibody has the advantage to overcome the absence of the anti-BRCA1 antibody epitope in truncated BRCA1 proteins. Tubulin was used as a loading control and was probed using an anti-Tubulin antibody on the same membrane after stripping the first labeling (bottom panel). In B and C, the cells analyzed were those in Figs. 4-5. (**D**) Absence of RNA pol II cleavage. Cells were grown in galactose for the indicated time and cell lysates were examined by Western blot for the presence of the RNA pol II protein. As shown in Fig. S10D, expression of BRCA1 is visualized after 30 min of galactose induction. Moreover, localization of BRCA1 in the yeast nucleus is observed after 1 hour of galactose induction (Fig. S10A), meaning that the 50 kDa cleaved part of the yeast RNA pol II (arrow) should be seen after 4 or 8 hours of galactose induction. Blue, neutral mutation; red, pathogenic mutation.

Table S1. Statistical analyses [a]

Figure	Comparison	Alternative hypothesis [b]	Sample size [c]	Test	*P*-value
1D	Vector and BRCA1	Difference between proportions	$n_{Vector} = 167$, $n_{BRCA1} = 167$	Fisher exact	1e-11
	Vector and BRCA1-mCherry	Difference between proportions	$n_{Vector} = 167$, $n_{BRCA1\text{-}mCherry} = 132$	Fisher exact	1e-9
2B	WT and NLSm	Difference between distributions	$n_{WT} = 314$, $n_{NLSm} = 372$	Fisher exact	7e-4
2C	WT and NLSm	$P(X_{NLSm} > X_{BRCA1}) > P(X_{NLSm} < X_{BRCA1})$	$n_{WT} = 3$, $n_{NLSm} = 3$	MWW	0.05
3B	WT and R1699W	Difference between distributions	$n_{WT} = 301$, $n_{R1699W} = 292$	Fisher exact	NS
	WT and R1751Q	Difference between distributions	$n_{WT} = 301$, $n_{R1751Q} = 295$	Fisher exact	NS
	WT and V1804D	Difference between distributions	$n_{WT} = 301$, $n_{V1804D} = 275$	Fisher exact	NS
	WT and P1859R	Difference between distributions	$n_{WT} = 301$, $n_{P1859R} = 323$	Fisher exact	NS
	WT and T1691K	Difference between distributions	$n_{WT} = 301$, $n_{T1691K} = 402$	Fisher exact	4e-14
	WT and G1706E	Difference between distributions	$n_{WT} = 301$, $n_{G1706E} = 379$	Fisher exact	5e-12
	WT and R1751P	Difference between distributions	$n_{WT} = 301$, $n_{R1751P} = 389$	Fisher exact	1e-4
	WT and W1837C	Difference between distributions	$n_{WT} = 301$, $n_{W1837C} = 345$	Fisher exact	7e-10
3C	WT and R1699W	$P(X_{R1699W} > X_{BRCA1}) > P(X_{R1699W} < X_{BRCA1})$	$n_{WT} = 3$, $n_{R1699W} = 3$	MWW	0.05
	WT and R1751Q	$P(X_{R1751Q} > X_{BRCA1}) > P(X_{R1751Q} < X_{BRCA1})$	$n_{WT} = 3$, $n_{R1751Q} = 3$	MWW	NS
	WT and V1804D	$P(X_{V1804D} > X_{BRCA1}) > P(X_{V1804D} < X_{BRCA1})$	$n_{WT} = 3$, $n_{V1804D} = 3$	MWW	0.05
	WT and P1859R	$P(X_{P1859R} > X_{BRCA1}) > P(X_{P1859R} < X_{BRCA1})$	$n_{WT} = 3$, $n_{P1859R} = 3$	MWW	NS
	WT and T1691K	$P(X_{T1691K} > X_{BRCA1}) > P(X_{T1691K} < X_{BRCA1})$	$n_{WT} = 3$, $n_{T1691K} = 3$	MWW	0.05
	WT and G1706E	$P(X_{G1706E} > X_{BRCA1}) > P(X_{G1706E} < X_{BRCA1})$	$n_{WT} = 3$, $n_{G1706E} = 3$	MWW	0.05
	WT and R1751P	$P(X_{R1751P} > X_{BRCA1}) > P(X_{R1751P} < X_{BRCA1})$	$n_{WT} = 3$, $n_{R1751P} = 3$	MWW	0.05
	WT and W1837C	$P(X_{W1837C} > X_{BRCA1}) > P(X_{W1837C} < X_{BRCA1})$	$n_{WT} = 3$, $n_{W1837C} = 3$	MWW	0.05
3D	WT and mCherry alone	Difference between distributions	$n_{WT} = 55$, $n_{mCherry\ alone} = 47$	Fisher exact	0.03
	WT and R1699W	Difference between distributions	$n_{WT} = 55$, $n_{R1699W} = 52$	Fisher exact	NS
	WT and R1751Q	Difference between distributions	$n_{WT} = 55$, $n_{R1751Q} = 56$	Fisher exact	NS
	WT and V1804D	Difference between distributions	$n_{WT} = 55$, $n_{V1804D} = 62$	Fisher exact	NS
	WT and P1859R	Difference between distributions	$n_{WT} = 55$, $n_{P1859R} = 56$	Fisher exact	NS
	WT and T1691K	Difference between distributions	$n_{WT} = 55$, $n_{T1691K} = 53$	Fisher exact	8e-9
	WT and G1706E	Difference between distributions	$n_{WT} = 55$, $n_{G1706E} = 48$	Fisher exact	3e-9
	WT and R1751P	Difference between distributions	$n_{WT} = 55$, $n_{R1751P} = 57$	Fisher exact	5e-6
	WT and W1837C	Difference between distributions	$n_{WT} = 55$, $n_{W1837C} = 58$	Fisher exact	2e-7
5C	WT and W1837C	Difference between distributions	$n_{WT} = 300$, $n_{W1837C} = 276$	Fisher exact	<2e-16
	WT and Y1853X	Difference between distributions	$n_{WT} = 300$, $n_{Y1853X} = 284$	Fisher exact	<2e-16
6A	WT and Vector	$P(X_{Vector} > X_{BRCA1}) > P(X_{Vector} < X_{BRCA1})$	$n_{WT} = 3$, $n_{Vector} = 3$	MWW	0.05
	WT and NLSm	$P(X_{NLSm} > X_{BRCA1}) > P(X_{NLSm} < X_{BRCA1})$	$n_{WT} = 3$, $n_{NLSm} = 3$	MWW	0.05
6B	WT and Vector	$P(X_{Vector} > X_{BRCA1}) > P(X_{Vector} < X_{BRCA1})$	$n_{WT} = 3$, $n_{Vector} = 3$	MWW	0.05
	WT and R1699W	$P(X_{R1699W} > X_{BRCA1}) > P(X_{R1699W} < X_{BRCA1})$	$n_{WT} = 3$, $n_{R1699W} = 3$	MWW	NS
	WT and R1751Q	$P(X_{R1751Q} > X_{BRCA1}) > P(X_{R1751Q} < X_{BRCA1})$	$n_{WT} = 3$, $n_{R1751Q} = 3$	MWW	NS
	WT and V1804D	$P(X_{V1804D} > X_{BRCA1}) > P(X_{V1804D} < X_{BRCA1})$	$n_{WT} = 3$, $n_{V1804D} = 3$	MWW	NS
	WT and P1859R	$P(X_{P1859R} > X_{BRCA1}) > P(X_{P1859R} < X_{BRCA1})$	$n_{WT} = 3$, $n_{P1859R} = 3$	MWW	NS
	WT and T1691K	$P(X_{T1691K} > X_{BRCA1}) > P(X_{T1691K} < X_{BRCA1})$	$n_{WT} = 3$, $n_{T1691K} = 3$	MWW	0.05
	WT and G1706E	$P(X_{G1706E} > X_{BRCA1}) > P(X_{G1706E} < X_{BRCA1})$	$n_{WT} = 3$, $n_{G1706E} = 3$	MWW	0.05
	WT and R1751P	$P(X_{R1751P} > X_{BRCA1}) > P(X_{R1751P} < X_{BRCA1})$	$n_{WT} = 3$, $n_{R1751P} = 3$	MWW	0.05
	WT and W1837C	$P(X_{W1837C} > X_{BRCA1}) > P(X_{W1837C} < X_{BRCA1})$	$n_{WT} = 3$, $n_{W1837C} = 3$	MWW	0.05
6C	WT and Vector	$P(X_{Vector} > X_{BRCA1}) > P(X_{Vector} < X_{BRCA1})$	$n_{WT} = 3$, $n_{Vector} = 3$	MWW	0.05
	WT and Central	$P(X_{Central} > X_{BRCA1}) > P(X_{Central} < X_{BRCA1})$	$n_{WT} = 3$, $n_{Central} = 3$	MWW	NS
	WT and Nter-Cter	$P(X_{Nter\text{-}Cter} > X_{BRCA1}) > P(X_{Nter\text{-}Cter} < X_{BRCA1})$	$n_{WT} = 3$, $n_{Nter\text{-}Cter} = 3$	MWW	0.05
	WT and Nter-NLS-Cter	$P(X_{Nter\text{-}NLS\text{-}Cter} > X_{BRCA1}) > P(X_{Nter\text{-}NLS\text{-}Cter} < X_{BRCA1})$	$n_{WT} = 3$, $n_{Nter\text{-}NLS\text{-}Cter} = 3$	MWW	0.05
6F	Spot and No-spot	Difference between proportions	$n_{Spot} = 28$, $n_{No\text{-}spot} = 24$	Chi2	3e-8
6G	WT and Vector	$P(X_{Vector} > X_{BRCA1}) \neq P(X_{Vector} < X_{BRCA1})$	$n_{WT} = 51$, $n_{Vector} = 127$	MWW	5e-6
7A	WT and Vector ADH1p	$P(X_{Vector} > X_{BRCA1}) > P(X_{Vector} < X_{BRCA1})$	$n_{WT} = 3$, $n_{Vector} = 3$	MWW	0.05
	WT and Vector GAL1p + 2µ	$P(X_{Vector} > X_{BRCA1}) > P(X_{Vector} < X_{BRCA1})$	$n_{WT} = 3$, $n_{Vector} = 3$	MWW	0.05
	WT and Vector inserted	$P(X_{Vector} > X_{BRCA1}) > P(X_{Vector} < X_{BRCA1})$	$n_{WT} = 3$, $n_{Vector} = 3$	MWW	NS
7D	GAL1p and ADH1p	Difference between distributions	$n_{GAL1p} = 188$, $n_{ADH1p} = 712$	Fisher exact	<2e-16

	WT and *ssa1Δssa2Δ*	Difference between distributions	n_{WT} = 303, $n_{ssa1\Delta ssa2\Delta}$ = 181	Fisher exact	7e-15
	WT and GPDp-HSP26	Difference between distributions	n_{WT} = 297, $n_{GPDp\text{-}HSP26}$ = 289	Fisher exact	0.02
S2	WT and GPDp-HSP104	Difference between distributions	n_{WT} = 202, $n_{GPDp\text{-}HSP104}$ = 251	Fisher exact	NS
	WT and Guanidine	Difference between distributions	n_{WT} = 210, $n_{Guanidine}$ = 254	Fisher exact	NS
	WT and *hsp104Δ*	Difference between distributions	n_{WT} = 252, $n_{hsp104\Delta}$ = 95	Fisher exact	NS
	WT and *atg8Δ*	Difference between distributions	n_{WT} = 204, $n_{atg8\Delta}$ = 302	Fisher exact	NS
S3	WT and *atg1Δ*	Difference between distributions	n_{WT} = 524, $n_{atg1\Delta}$ = 534	Fisher exact	NS
	WT and *ump1Δ*	Difference between distributions	n_{WT} = 267, $n_{ump1\Delta}$ = 299	Fisher exact	0.02
	WT and mCherry alone	Difference between distributions	n_{WT} = 64, $n_{mCherry\ alone}$ = 64	Fisher exact	0.006
	WT and R1699W	Difference between distributions	n_{WT} = 64, n_{R1699W} = 63	Fisher exact	NS
	WT and R1751Q	Difference between distributions	n_{WT} = 64, n_{R1751Q} = 65	Fisher exact	NS
	WT and V1804D	Difference between distributions	n_{WT} = 64, n_{V1804D} = 69	Fisher exact	NS
S7A	WT and P1859R	Difference between distributions	n_{WT} = 64, n_{P1859R} = 64	Fisher exact	NS
	WT and T1691K	Difference between distributions	n_{WT} = 64, n_{T1691K} = 46	Fisher exact	3e-5
	WT and G1706E	Difference between distributions	n_{WT} = 64, n_{G1706E} = 50	Fisher exact	5e-5
	WT and R1751P	Difference between distributions	n_{WT} = 64, n_{R1751P} = 69	Fisher exact	0.01
	WT and W1837C	Difference between distributions	n_{WT} = 64, n_{W1837C} = 66	Fisher exact	2e-6
	WT and mCherry alone	Difference between distributions	n_{WT} = 55, $n_{mCherry\ alone}$ = 47	Fisher exact	1e-7
	WT and R1699W	Difference between distributions	n_{WT} = 55, n_{R1699W} = 52	Fisher exact	NS
	WT and R1751Q	Difference between distributions	n_{WT} = 55, n_{R1751Q} = 55	Fisher exact	NS
	WT and V1804D	Difference between distributions	n_{WT} = 55, n_{V1804D} = 62	Fisher exact	NS
S7B	WT and P1859R	Difference between distributions	n_{WT} = 55, n_{P1859R} = 56	Fisher exact	NS
	WT and T1691K	Difference between distributions	n_{WT} = 55, n_{T1691K} = 53	Fisher exact	8e-10
	WT and G1706E	Difference between distributions	n_{WT} = 55, n_{G1706E} = 48	Fisher exact	7e-10
	WT and R1751P	Difference between distributions	n_{WT} = 55, n_{R1751P} = 58	Fisher exact	3e-6
	WT and W1837C	Difference between distributions	n_{WT} = 55, n_{W1837C} = 58	Fisher exact	6e-9
	WT and mCherry alone	Difference between distributions	n_{WT} = 64, $n_{mCherry\ alone}$ = 65	Fisher exact	5e-8
	WT and R1699W	Difference between distributions	n_{WT} = 64, n_{R1699W} = 64	Fisher exact	NS
	WT and R1751Q	Difference between distributions	n_{WT} = 64, n_{R1751Q} = 65	Fisher exact	NS
	WT and V1804D	Difference between distributions	n_{WT} = 64, n_{V1804D} = 69	Fisher exact	NS
S7C	WT and P1859R	Difference between distributions	n_{WT} = 64, n_{P1859R} = 64	Fisher exact	NS
	WT and T1691K	Difference between distributions	n_{WT} = 64, n_{T1691K} = 46	Fisher exact	2e-5
	WT and G1706E	Difference between distributions	n_{WT} = 64, n_{G1706E} = 50	Fisher exact	3e-4
	WT and R1751P	Difference between distributions	n_{WT} = 64, n_{R1751P} = 68	Fisher exact	0.009
	WT and W1837C	Difference between distributions	n_{WT} = 64, n_{W1837C} = 65	Fisher exact	1e-6
S8B	WT and Vector	Difference between proportions	n_{WT} = 150, n_{Vector} = 164	Chi2	2e-14
S8C	WT and Vector	Difference between distributions	n_{WT} = 98, n_{Vector} = 37	Chi2	9e-4
S8D	WT and Vector	Difference between proportions	n_{WT} = 150, n_{Vector} = 164	Chi2	<2e-16
S8E	WT and Vector	$P(X_{Vector} > X_{BRCA1}) \neq P(X_{Vector} < X_{BRCA1})$	n_{WT} = 145, n_{Vector} = 162	MWW	<2e-16
	0 min and 30 min	Difference between distributions	$n_{0\ min}$ = 621, $n_{30\ min}$ = 607	Fisher exact	4e-9
	0 min and 1 h	Difference between distributions	$n_{0\ min}$ = 621, n_{1h} = 575	Fisher exact	<2e-16
S12F	0 min and 2 h	Difference between distributions	$n_{0\ min}$ = 621, n_{2h} = 615	Fisher exact	<2e-16
	0 min and 4 h	Difference between distributions	$n_{0\ min}$ = 621, n_{4h} = 657	Fisher exact	<2e-16
	2h CHX and 2 h Ethanol	Difference between distributions	$n_{2h\ CHX}$ = 615, $n_{2h\ Ethanol}$ = 571	Fisher exact	<2e-16
S12H	0 min and 4 h	Difference between distributions	$n_{0\ min}$ = 683, n_{4h} = 548	Fisher exact	<2e-16
	4h CHX and 4 h Ethanol	Difference between distributions	$n_{2h\ CHX}$ = 548, $n_{2h\ Ethanol}$ = 606	Fisher exact	<2e-16
S13E	DMSO and MG132	Difference between distributions	n_{DMSO} = 549, n_{MG132} = 575	Fisher exact	5e-5
S13G	DMSO and MG132	Difference between distributions	n_{DMSO} = 524, n_{MG132} = 596	Fisher exact	4e-5

[a] n, sample size for each class tested; MWW, Mann-Whitney-Wilcoxon; NS, non significant

[b] For the MWW test, quantitative variable distributions are unknown in the statistical population. Therefore, alternative hypotheses refer to the tendency for values in the tested class to be larger than in the control class (in the first row of Fig. 6A, the probability $P(X_{Vector} > X_{BRCA1})$, that a value in the Vector class is greater than a value in the BRCA1 class, is greater than the probability $P(X_{Vector} < X_{BRCA1})$ that a value in the Vector class is lower than a value in the BRCA1 class).

[c] When Fisher exact tests involved two or more independent clones, the sample size median was used.

Table S2. Correlations between structural stability and functional data

Strain	LM	SF	YL	Structural stability
BRCA1	0.144	0.32011331	0.03011169	100
M1652I	0.141	0.33056577	0.019508914	79
M1652T	0.195	0.31916635	0.033521303	84
F1662S	0.130	0.32405386	0.033474118	121
A1669S	0.158	0.30219840	0.007331425	70
E1682K	0.148	0.31781733	0.004404384	92
T1685A	0.338	0.10702164	0.412329078	18
T1685I	0.387	0.16315550	0.439432238	13
M1689R	0.388	0.09630668	0.781520693	20
R1699W	0.154	0.35398230	0.014217152	90
G1706E	0.397	0.08198442	0.984477893	2
A1708E	0.368	0.09740219	0.973875384	4
S1715R	0.387	0.09555141	0.994699804	1
T1720A	0.142	0.34723473	0.004224351	74
G1738R	0.295	0.20485484	0.445016465	2
R1751Q	0.128	0.32063492	0.018504379	59
L1764P	0.361	0.16589620	0.743579501	18
I1766S	0.393	0.13080603	0.968397449	0
M1775K	0.170	0.37789528	0.007123580	103
M1775R	0.177	0.28772290	0.013772868	48
G1788V	0.407	0.17286119	0.997409639	0
V1804D	0.158	0.35462842	0.001647348	89
V1838E	0.405	0.19506031	1.000000000	8
P1859R	0.144	0.32621083	0.002212185	105

The structural stability values are published by Lee et al., 2010, and the other values by Thouvenot et al., 2016. LM, Liquid Medium (OD600 which reflects growth rate); SF, Spot Formation (proportion of cells showing a single fluorescent spot); YL, Yeast Localization (proportion of cytoplasmic spots).

Table S3. Plasmids used in this study

Name	cDNA	HGVS nomenclature[a]	Source
pJL48	None (Vector)		Millot et al., 2011
pJL45	BRCA1		Millot et al., 2011
pGM13	mCherry		Millot et al., 2011
pGM40	BRCA1-mCherry		Millot et al., 2011
pVL47	BRCA1-GFP		This study
pGM108	NLSm-mCherry	c.[1507_1508delAAinsGC; 1510_1511delCGinsGC; 1513_1514delAAinsGC; 1516_1517delAGinsGC; 1822_1823delAAinsGC; 1828_1829delAGinsGC; 1834_1835delAGinsGC; 1837_1838delAGinsGC] which correspond to K503A-R504A-K505A-R506A and K608A-R610A-R612A-R613A	This study
pPT75	T1691K-mCherry	c.5072 C>A	This study
pPT76	G1706E-mCherry	c.5117 G>A	This study
pPT79	R1751P-mCherry	c.5252 G>C	This study
pPT80	W1837C-mCherry	c.5511 G>T	This study
pPT213	R1699W-mCherry	c.5095C>T	This study
pPT217	R1751Q-mCherry	c.5252G>A	This study
pPT218	V1804D-mCherry	c.5411T>A	This study
pPT84	P1859R-mCherry	c.5576C>G	This study
pPT70	T1691K	c.5072 C>A	This study
pPT71	G1706E	c.5117 G>A	This study
pPT72	R1751P	c.5252 G>C	This study
pPT73	W1837C	c.5511 G>T	This study
pPT209	R1699W	c.5095C>T	This study
pPT210	R1751Q	c.5252G>A	This study
pPT211	V1804D	c.5411T>A	This study
pPT82	P1859R	c.5576C>G	This study
pGM95	Central-mCherry	c.[4_300del; 4954_5592del]; p.[D2_E100del; M1652_Y1863del]	This study
pGM107	Nter-Cter-mCherry	c.301_4866del; p.Y101_L1639del	This study
pGM102	Nter-NLS-Cter-mCherry	c.[301_1482del; 1549_4866del]; p.[Y101_Q494del; F517_L1639del]	This study
pGM105	NLSm	idem pGM108	This study
pGM94	Central	c.[4_300del; 4954_5592del]; p.[D2_E100del; M1652_Y1863del]	This study
pGM106	Nter-Cter	c.301_4866del; p.Y101_L1639del	This study
pGM101	Nter-NLS-Cter	c.[301_1482del; 1549_4866del]; p.[Y101_Q494del; F517_L1639del]	This study
pGM136	Nter-NLS-Cter-W1837C-mCherry	c.[301_1482del; 1549_4866del; 5511 G>T]	This study
pGM135	Nter-NLS-Cter-Y1853X-mCherry	c.[301_1482del; 1549_4866del; 5559C>A]	This study
pGM35	ADH1p alone		This study
pGM36	ADH1p-BRCA1		This study
pGM96	ADH1p-BRCA1-mCherry		This study
pGM137	CMVp-mCherry		This study
pGM140	CMVp-mCherry-BRCA1		This study
pBB9	CMVp-mCherry-T1691K	c.5072 C>A	This study
pBB10	CMVp-mCherry-G1706E	c.5117 G>A	This study
pBB11	CMVp-mCherry-R1751P	c.5252 G>C	This study
pBB12	CMVp-mCherry-W1837C	c.5511 G>T	This study
pBB14	CMVp-mCherry-R1699W	c.5095C>T	This study
pBB15	CMVp-mCherry-R1751Q	c.5252G>A	This study
pBB16	CMVp-mCherry-V1804D	c.5411T>A	This study
pBB13	CMVp-mCherry-P1859R	c.5576C>G	This study
pJL62	GAL1p alone		This study
pJL59	GAL1p-BRCA1		This study

[a]Mutation and deletion nomenclature according to the human genome variation society (http://www.hgvs.org/mutnomen/). The *BRCA1* cDNA used in this study corresponds to the AY888184.1 GenBank sequence. Unless otherwise indicated, the promoter used is *GAL1p*.

Table S4. Yeast strains used in this study

Strain designation	Common name	Genotype	Source
BY4741		*MAT* a, *leu2Δ0, his3Δ1, ura3Δ0, met15Δ0*	Winzeler et al., 1999
BY4742		*MAT* α, *leu2Δ0, his3Δ1, ura3Δ0, lys2Δ0*	Winzeler et al., 1999
ORT5057		BY4741, *trp1::kanMX*	This study
YKR082W-GFP	Nup133-GFP	*MAT* a, *leu2Δ0, his3Δ1, ura3Δ0, met15Δ0, nup133::NUP133-GFP(HIS3MX6)*	Huh et al., 2003
GMT130	Nup133-GFP mCherry	YKR082W-GFP + pGM13	Millot et al., 2011
GMT083	Nup133-GFP BRCA1-mCherry	YKR082W-GFP + pGM40	Millot et al., 2011
YOL038W-GFP	Pre6-GFP	*MAT* a, *leu2Δ0, his3Δ1, ura3Δ0, met15Δ0, pre6::PRE6-GFP(HIS3MX6)*	Huh et al., 2003
GMT188	Pre6-GFP Vector	YOL038W-GFP + pJL48	This study
GMT189	Pre6-GFP BRCA1	YOL038W-GFP + pJL45	This study
GMT037	Pre6-GFP BRCA1-mCherry	YOL038W-GFP + pGM40	This study
ORT5894	BRCA1-GFP	BY4742 + pVL47	This study
GMT353	Nup133-GFP NLSm-mCherry	YKR082W-GFP + pGM108	This study
YGL122C-GFP	Nab2-GFP	*MAT* a, *leu2Δ0, his3Δ1, ura3Δ0, met15Δ0, nab2::NAB2-GFP(HIS3MX6)*	Huh et al., 2003
GMT002	Nab2-GFP BRCA1-mCherry	YGL122C-GFP + pGM40	This study
YOR048C-GFP	Rat1-GFP	*MAT* a, *leu2Δ0, his3Δ1, ura3Δ0, met15Δ0, rat1::RAT1-GFP(HIS3MX6)*	Huh et al., 2003
GMT035	Rat1-GFP BRCA1-mCherry	YOR048C-GFP + pGM40	This study
YDL140C-GFP	Rpo21-GFP	*MAT* a, *leu2Δ0, his3Δ1, ura3Δ0, met15Δ0, rpo21::RPO21-GFP(HIS3MX6)*	Huh et al., 2003
GMT012	Rpo21-GFP BRCA1-mCherry	YDL140C-GFP + pGM40	This study
YGR135W-GFP	Pre9-GFP	*MAT* a, *leu2Δ0, his3Δ1, ura3Δ0, met15Δ0, pre9::PRE9-GFP(HIS3MX6)*	Huh et al., 2003
GMT295	Pre9-GFP BRCA1-mCherry	YGR135W-GFP + pGM40	This study
Y01514	*hsp104Δ*	*MAT* a, *leu2Δ0, his3Δ1, ura3Δ0, met15Δ0, hsp104Δ*::KanMX	Winzeler et al., 1999
GMT242	*hsp104Δ* BRCA1-mCherry	Y01514 + pGM40	This study
ORT6691	BRCA1-mCherry	BY4741 + pGM40	Millot et al., 2011
GMT253	GPDp-HSP104 Nup133-GFP	*MAT* a, *leu2Δ0, his3Δ1, ura3Δ0, met15Δ0, nup133::NUP133-GFP(HIS3MX6), hsp104p::GPDp(NatNT2)*	This study
GMT260	GPDp-HSP104 Nup133-GFP BRCA1-mCherry	GMT260 + pGM40	This study
GMT320	*ssa1Δssa2Δ*	*MATa, leu2Δ0, his3Δ1, ura3Δ0, met15Δ0, ssa1Δ::HphMX, ssa2Δ::KanMX*	This study
GMT357	*ssa1Δssa2Δ* BRCA1-mCherry	GMT320 + pGM40	This study
GMT406	GPDp-HSP26 Nup133-GFP	*MAT* a, *leu2Δ0, his3Δ1, ura3Δ0, met15Δ0, nup133::NUP133-GFP(HIS3MX6), hsp26p::GPDp(kanMX4)*	This study
GMT420	GPDp-HSP26 Nup133-GFP BRCA1-mCherry	GMT406 + pGM40	This study
Y03104	*atg8Δ*	*MAT* a, *leu2Δ0, his3Δ1, ura3Δ0, met15Δ0, atg8Δ*::KanMX	Winzeler et al., 1999
GMT408	*atg8Δ* BRCA1-mCherry	Y03104 + pGM40	This study
Y04547	*atg1Δ*	*MAT* a, *leu2Δ0, his3Δ1, ura3Δ0, met15Δ0, atg1Δ*::KanMX	Winzeler et al., 1999
GMT536	*atg1Δ* BRCA1-mCherry	Y04547 + pGM40	This study
BLT67	*ump1Δ*	*MAT* α, *leu2Δ0, his3Δ1, ura3Δ0, lys2Δ0, ump1Δ::hphMX4*	Le Tallec et al., 2007
GMT389	*ump1Δ* BRCA1-mCherry	BLT67 + pGM40	This study
YLL026W-GFP	Functional Hsp104-GFP	*MAT* a, *leu2Δ0, his3Δ1, ura3Δ0, met15Δ0, hsp104::HSP104-GFP(HIS3MX6)*	Provided by Michel Toledano
GMT517	Hsp104-GFP BRCA1-mCherry	YLL026W-GFP + pGM40	This study
GMT518	Hsp104-GFP NLSm-mCherry	YLL026W-GFP + pGM108	This study
YAL005C-GFP	Ssa1-GFP	*MAT* a, *leu2Δ0, his3Δ1, ura3Δ0, met15Δ0, ssa1::SSA1-GFP(HIS3MX6)*	Huh et al., 2003
GMT238	Ssa1-GFP BRCA1-mCherry	YAL005C-GFP + pGM40	This study
GMT452	Ssa1-GFP NLSm-mCherry	YAL005C-GFP + pGM108	This study
GMT387	Nup133-GFP T1691K-mCherry	YKR082W-GFP + pPT75	This study
GMT388	Nup133-GFP G1706E-mCherry	YKR082W-GFP + pPT76	This study
GMT374	Nup133-GFP R1751P-mCherry	YKR082W-GFP + pPT79	This study
GMT375	Nup133-GFP W1837C-mCherry	YKR082W-GFP + pPT80	This study
GMT516	Nup133-GFP R1699W-mCherry	YKR082W-GFP + pPT213	This study
GMT496	Nup133-GFP R1751Q-mCherry	YKR082W-GFP + pPT217	This study
GMT497	Nup133-GFP V1804D-mCherry	YKR082W-GFP + pPT218	This study
GMT376	Nup133-GFP P1859R-mCherry	YKR082W-GFP + pPT84	This study
GMT317	Nup133-GFP Central-mCherry	YKR082W-GFP + pGM95	This study
GMT352	Nup133-GFP Nter-Cter-mCherry	YKR082W-GFP + pGM107	This study
GMT351	Nup133-GFP Nter-NLS-Cter-mCherry	YKR082W-GFP + pGM102	This study
GMT422	Nup133-GFP Nter-NLS-Cter-W1837C-mCherry	YKR082W-GFP + pGM136	This study
GMT421	Nup133-GFP Nter-NLS-Cter-Y1853X-mCherry	YKR082W-GFP + pGM135	This study
ORT5039	Vector	BY4741 + pJL48	Millot et al., 2011
ORT5034	BRCA1	BY4741 + pJL45	Millot et al., 2011
GMT337	NLSm	BY4741 + pGM105	This study
GMT369	T1691K	BY4741 + pPT70	This study
GMT370	G1706E	BY4741 + pPT71	This study
GMT371	R1751P	BY4741 + pPT72	This study
GMT372	W1837C	BY4741 + pPT73	This study
GMT512	R1699W	BY4741 + pPT209	This study
GMT492	R1751Q	BY4741 + pPT210	This study
GMT513	V1804D	BY4741 + pPT211	This study
GMT373	P1859R	BY4741 + pPT82	This study
GMT319	Central	BY4741 + pGM94	This study
GMT350	Nter-Cter	BY4741 + pGM106	This study
GMT349	Nter-NLS-Cter	BY4741 + pGM101	This study
ORT5061	GAL1p single copy inserted (Vector)	ORT5057, *trp1::pJL62(TRP1)*	This study
ORT5059	GAL1p-BRCA1 single copy inserted	ORT5057, *trp1::pJL59(TRP1)*	This study
ORT6695	ADH1p alone	BY4741 + pGM35	This study
ORT6690	ADH1p-BRCA1	BY4741 + pGM36	This study
GMT316	Nup133-GFP ADH1p-BRCA1-mCherry	YKR082W-GFP + pGM96	This study
Y02409	*pdr5Δ*	*MAT* a, *leu2Δ0, his3Δ1, ura3Δ0, met15Δ0, pdr5Δ*::KanMX	Winzeler et al., 1999
GMT451	*pdr5Δ* BRCA1-mCherry	Y02409 + pGM40	This study
GMT596	*pdr5Δ* T1691K-mCherry	Y02409 + pPT75	This study
GMT597	*pdr5Δ* R1751Q-mCherry	Y02409 + pPT217	This study

Supplementary Figure and Movie legends

Figs. S5-S14 are available at:
http://xfer.curie.fr/get/mKbctRQTCl1/Supplementary_Figures_S5_to_S14.pdf

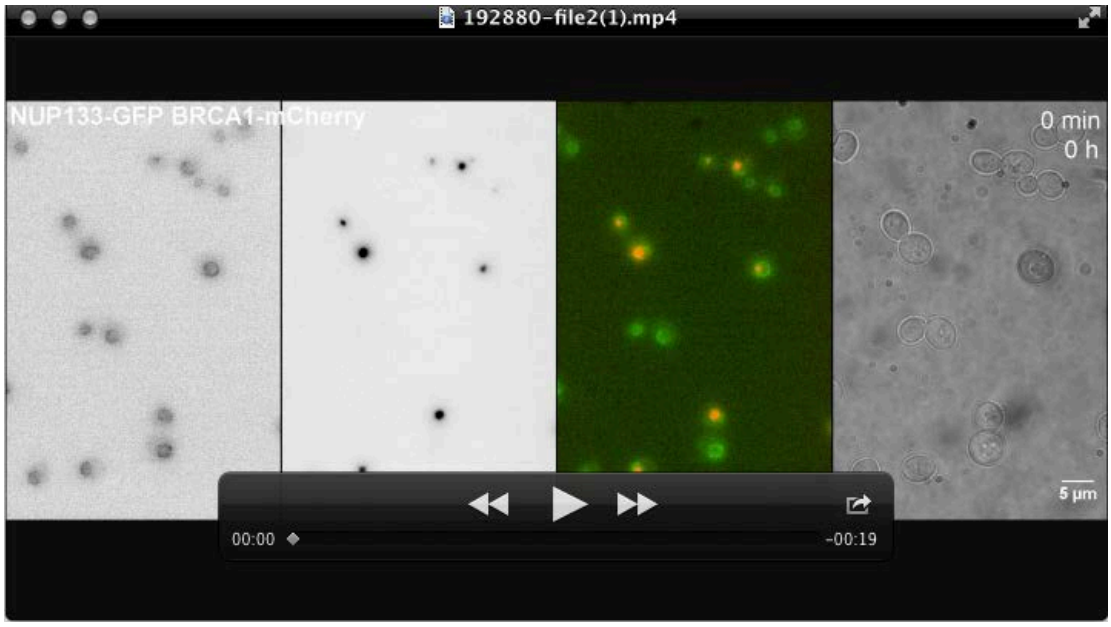

Movie S1. Yeast cells exhibiting the BRCA1 aggregate are blocked in G1. NUP133-GFP cells expressing BRCA1-mCherry were pre-stimulated with galactose for 4 hours, spread on a slide covered with an agarose pad containing galactose and immobilized with a coverslip. Then, galactose stimulation was monitored by fluorescent videomicroscopy for 6 more hours. Movies were analyzed by spotting isolated cells at the beginning of the record, called "mother cells" and by measuring different parameters of these mother cells.

Movie S2. Cells expressing BRCA1 form a mix of non-dividing and slow dividing cells. Cells were pre-stimulated with galactose for 4 hours, spread on a slide covered with an agarose pad containing galactose and immobilized with a coverslip. Vector cells were used as a control. Then, galactose (GAL) stimulation was monitored using transillumination videomicroscopy for 9 more hours. Movies were analyzed as in **Movie S1**.

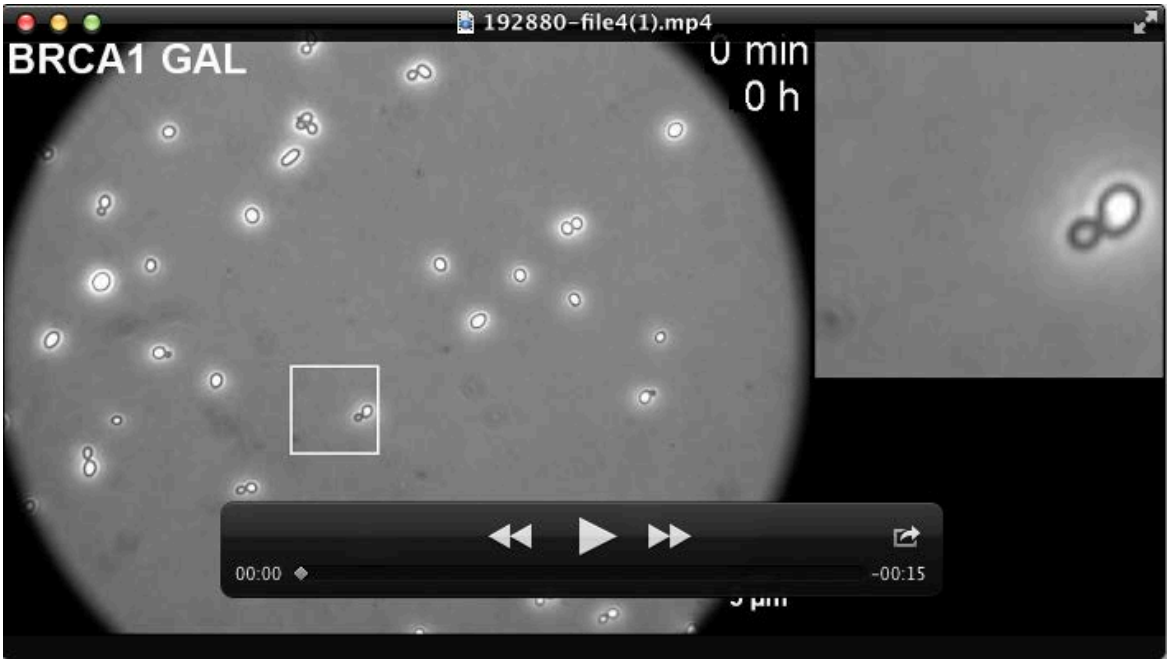

Movie S3. Example of cell division time. Magnification of Movie S2 (BRCA1), showing the rotation of the mother and daughter cells at the end of the division process. This rotating event, indicated by arrows, is used as starting and ending points of cell division time. In this example, the cell division time is 324 - 72 = 252 minutes.